

Unified analysis of Topological Defects in 2D systems of Active and Passive disks

Pasquale Digregorio,^{1,2} Demian Levis,^{3,4} Leticia F. Cugliandolo,^{5,6}
Giuseppe Gonnella,¹ and Ignacio Pagonabarraga^{2,4}

¹*Dipartimento di Fisica, Università degli Studi di Bari and INFN,
Sezione di Bari, via Amendola 173, Bari, I-70126, Italy*

²*Centre Européen de Calcul Atomique et Moléculaire (CECAM),
Ecole Polytechnique Fédérale de Lausanne (EPFL),
Batochimie, Avenue Forel 2, 1015 Lausanne, Switzerland*

³*Departament de Física de la Materia Condensada,
Universitat de Barcelona, Martí i Franquès 1, 08028 Barcelona, Spain*

⁴*UBICS University of Barcelona Institute of Complex Systems, Martí i Franquès 1, E08028 Barcelona, Spain*

⁵*Sorbonne Université, Laboratoire de Physique Théorique et Hautes Energies,
CNRS UMR 7589, 4 Place Jussieu, 75252 Paris Cedex 05, France*

⁶*Institut Universitaire de France, 1 rue Descartes, 75231 Paris Cedex 05 France
(Dated: December 21, 2021)*

We provide a comprehensive quantitative analysis of localized and extended topological defects in the steady state of 2D passive and active repulsive Brownian disk systems. We show that, both in and out-of-equilibrium, the passage from the solid to the hexatic is driven by the unbinding of dislocations, in quantitative agreement with the KTHNY singularity. Instead, although disclinations dissociate as soon as the liquid phase appears, extended clusters of defects largely dominate below the solid-hexatic critical line. The latter percolate in the liquid phase very close to the hexatic-liquid transition, both for continuous and discontinuous transitions, in the homogeneous liquid regime. At critical percolation the clusters of defects are fractal with statistical and geometric properties that, within our numerical accuracy, are independent of the activity and compatible with the universality class of uncorrelated critical percolation. We also characterize the spatial organization of different kinds of point-like defects and we show that the disclinations are not free, but rather always very near more complex defect structures. At high activity, the bulk of the dense phase generated by Motility-Induced Phase Separation is characterized by a density of point-like defects, and statistics and morphology of defect clusters, set by the amount of activity and not the packing fraction. Hexatic domains within the dense phase are separated by grain-boundaries along which a finite network of topological defects resides, interrupted by gas bubbles in cavitation. The fractal dimension of this network diminishes for increasing activity. This structure is dynamic in the sense that the defect network allows for an unzipping mechanism that leaves free space for gas bubbles to appear, close, and even be released into the dilute phase.

I. INTRODUCTION

In two-dimensions (2D) thermal fluctuations often prevent the emergence of Long-Range Order (LRO), as illustrated by the absence of spontaneous magnetization in 2D Heisenberg magnets [1] and positional order in 2D particle systems [2]. However, unconventional phase transitions driven by topological defects can still occur: for example, in 2D planar magnets, the binding-unbinding of vortices drive the so-called Berezinskii-Kosterlitz-Thouless (BKT) transition between a paramagnet and a low temperature critical phase with Quasi-Long-Range Order (QLRO) [3, 4].

The nature of the melting transition in 2D is far more involved and controversial than the BKT magnetic one [5–10], partly due to the fact that particle systems might have two types of order, translational and orientational, and thus two kinds of topological defects: dislocations and disclinations. The most standard picture of 2D melting in spherically symmetric particle systems follows the work of Kosterlitz-Thouless-Halperin-Nelson-Young (KTHNY) [11–13], according to which the transition from the solid (with positional QLRO and orienta-

tional LRO) to the isotropic liquid, occurs in two-steps, separated by an intermediate hexatic phase characterized by orientational QLRO. In this picture, these solid-hexatic and hexatic-liquid transitions are of BKT type, driven by the unbinding of dislocations and disclinations, respectively. While evidence for the KTHNY scenario was given by some experiments [14] and simulations [15–18], alternative mechanisms were proposed [5, 6]. In particular, one in which the continuous two-step scenario is preempted by a single solid-liquid first-order transition driven by the aggregation of defects into grain-boundary-like structures [19–21]. Recent simulations [22–27] (see also [28]) and experiments [29] showed that the melting of equilibrium passive repulsive disks shares aspects of both scenarios: a BKT solid-hexatic transition but a first-order hexatic-liquid one, if the interaction potential is stiff enough. It was thus suggested that the disclination-unbinding mechanism should be preempted by a first-order transition involving the proliferation of clusters of defects forming a percolating network in the liquid regime [17, 23, 25]. The mechanism for the hexatic-liquid transition should then be similar to the one controlling melting in 3D colloidal crystals, i.e., the growth of the

liquid along grain-boundaries [10, 30] (in this case delimiting regions with different hexatic order). Yet, neither a quantitative analysis of such clusters nor the derivation of a theory for the stability of the hexatic phase against grain-boundaries have been conducted. Moreover, and surprisingly enough, no clear experimental evidence and little numerical one [25, 31, 32] for dislocation unbinding at the solid-hexatic transition exists.

Besides the issues that still remain unclear for passive particle systems, the classical problem of 2D phase transitions is experiencing a resurgence of interest in the context of active matter systems. These are collections of self-propelled particles which pump energy from their environment and convert it into motion in the presence of dissipation, in a way that breaks detailed balance. Different aspects and approaches to active matter have been extensively reviewed in the literature [33–50]. Recently, it has been shown that self-propelled hard disks follow the two-step melting scenario of their passive counterparts at weak activities, up to a threshold above which hexatic-liquid coexistence, characteristic of the first-order nature of the transition, disappears [24] (see the phase diagram in Fig. 1). Both the hexatic-liquid and solid-hexatic transitions are shifted to higher densities as the degree of activity is increased and, at sufficiently high energy injection, these transitions overlap with a coexistence region purely triggered by self-propulsion, the so-called Motility-Induced Phase-Separation (MIPS) [41, 51–57]. Although topological defects are known to be crucial to grasp 2D equilibrium phase transitions, little attention has been paid to the study of how they influence phase transitions in active systems [58–61].

In this paper we shed new light on the 2D melting mechanism, both in- and out-of-equilibrium. With a huge computational effort we collected enough numerical data to perform a thorough quantitative analysis of the full spectrum of topological defects in systems of passive and active repulsive Brownian disks. Besides a careful analysis of point-like defects, we also characterize more complex structures, in the form of networks of strings and extended clusters of defects. Worthy of note is that we work in regimes in which the topological defects are numerous and of different kind, and it would be very hard, if not impossible, to follow their individual temporal evolution, contrary to what is sometimes possible to do in studies of active nematics [62–69].

Let us summarize here our results. We first show that the solid-hexatic transition is driven by the unbinding of dislocations and agrees, even *quantitatively*, with the KTHNY scenario at all activities. Although we see dislocation unbinding and hence proliferation of disclinations as soon as the liquid phase appears, either in coexistence or through a continuous phase transition, we find that 2D melting is generically accompanied by the *percolation* of clusters of topological defects close to the hexatic-liquid transition, both for active and passive systems. The presence of a spanning cluster, with similar properties to the ones of critical percolation, seems to be independent of

the order of the transition, and thus constitutes a fundamental feature of the melting of the hexatic. At critical percolation, the nature and geometry of the clusters are independent of activity within our numerical accuracy. We complement the study of the point-like defect number densities with the one of the defect-defect spatial correlations. This allows us to grasp the spatial organization of different kinds of point-like defects and, in particular, the preferred distance between them. We prove in this way that disclinations are not free but lie close to more complex defect structures at the interesting high densities where the thermodynamic transition takes place. Finally, we focus on the MIPS phase and we demonstrate that the defects are mostly located along grain boundaries between regions with different local orientational order. These give rise to a sort of unzipping dynamic mechanism that leaves free space for gas bubbles to cavitate. The size of this network does not scale with the size of the dense phase since the bubbles interrupt its connectivity. Consistently with other measurements, the properties of the defects in MIPS do not depend on the packing fraction at fixed activity.

The layout of the paper is the following. In Sec. II we introduce the model and the numerical methods. Section III is devoted to the definition and computational identification of all kinds of topological defects. We also recall the definition of several observables and critical percolation properties. We have chosen to order the following Sections in a way that goes from the analysis of the simpler point-like defects to the one of the larger structures. In Sec. IV we focus on the study of dislocations and disclinations, and their influence on the solid-hexatic and hexatic-liquid transitions, respectively. The MIPS phase and its network of strings of defects are studied in Sec. V. The properties of the defect clusters, their percolation, and its interplay with the melting mechanism are analyzed in Sec. VI. Finally, we close the paper in Sec. VII, where we put our results in the context of generic melting studies on the one hand, and we explain how the topological defect organization in MIPS relates to the micro hexatic phase separation on the other. We also make a short summary of our findings in this Section. Several Appendices complement our analysis.

II. MODEL AND METHODS

In this Section we present the model of Active Brownian Particles [52, 70, 71], we discuss the numerical methods employed, and we recall the Péclet number – packing fraction phase diagram at fixed temperature [24], focusing on the regime of variation of parameters that will be relevant to our study.

A. Active Brownian Particles

We consider N Active Brownian Particles (ABP) located at the positions \mathbf{r}_i in an $L_x \times L_y$ rectangular box with periodic boundary conditions (PBC) and obeying

$$\begin{aligned} m\ddot{\mathbf{r}}_i + \gamma\dot{\mathbf{r}}_i &= F_{\text{act}}\mathbf{n}_i - \sum_{j(\neq i)} \nabla_i U(r_{ij}) \\ &\quad + \sqrt{2\gamma k_B T} \boldsymbol{\xi}_i, \\ \dot{\theta}_i &= \sqrt{2D_\theta} \eta_i, \end{aligned} \quad (1)$$

where F_{act} is the self-propulsion force acting along the time-dependent direction $\mathbf{n}_i = (\cos \theta_i, \sin \theta_i)$, $r_{ij} = |\mathbf{r}_i - \mathbf{r}_j|$ is the inter-particle distance, and $U(r)$ is a repulsive potential. We consider two cases: (i) a hardcore form

$$U^H(r) = 4\varepsilon[(\sigma/r)^{64} - (\sigma/r)^{32}] + \varepsilon \quad (2)$$

if $r < \sigma_d = 2^{1/32}\sigma$ and 0 otherwise or (ii) a soft one [23]

$$U^S(r) = \varepsilon(\sigma_d/r)^6 \quad (3)$$

if $r < 2.6\sigma_d$ and 0 otherwise. The components of $\boldsymbol{\xi}$ and η are zero-mean and unit variance independent white Gaussian noises. We fixed $D_\theta = 3k_B T/(\sigma_d^2 \gamma)$. A constant persistence time $\tau_P = 1/D_\theta$ gives a persistence length $l_P = F_{\text{act}}\tau_P/\gamma$. We vary the packing fraction $\phi = \pi\sigma_d^2 N/(4L_x L_y)$, where $L_x/L_y = 2/\sqrt{3}$ (to allow for perfect hexagonal sphere packing), and the Péclet number $\text{Pe} = F_{\text{act}}\sigma_d/(k_B T)$. The persistence length is $l_P = \text{Pe}\sigma_d/3$ and grows proportionally to the Péclet number. Lengths and energies are later measured in units of σ_d and ε , respectively. The friction coefficient and the mass are set to $\gamma = 10$ and $m = 1$, consistently with an over-damped description. The temperature T controls the translational and orientational noise-noise temporal delta-correlations and was held fixed to $k_B T = 0.05$ for the hard potential case and $k_B T = 1$ for the soft one. In most of the simulations $N = 512^2$.

B. Numerical simulations

We used a velocity Verlet algorithm in the NVT ensemble that solves Newton's equations of motion with the addition of two force terms, a friction and a noise, which mimic a Langevin-type thermostat. The number of particles N and the volume V are fixed externally. The algorithm integrates numerically the stochastic evolution.

We used perfectly ordered initial conditions — with the disks arranged on a triangular lattice of a given spacing yielding the desired global surface fraction — because they relax faster towards stationarity in dense cases, the ones on which we are mainly interested in, rather than disordered packings. We ensured that the analysis is performed in the steady state limit.

Concerning the numerical methods, we parallelized the numerical computation with the help of the open source

software Large-scale Atomic/Molecular Massively Parallel Simulator (LAMMPS), available at www.github.com/lammps.

We adapted the time-step of integration, Δt , to enforce numerical stability. In this study, we gradually reduced the value of Δt in Molecular Dynamics simulation time units (MDs) for increasing Pe . For systems at $0 \leq \text{Pe} \leq 10$ we used $\Delta t = 0.005$, for $10 < \text{Pe} \leq 50$ we used $\Delta t = 0.002$, while for $\text{Pe} > 50$ we used the smallest time-step $\Delta t = 0.001$. Typical simulations took 50×10^4 MDs to ensure stationarity. As a rule, we let the system further evolve in the stationary regime for 50×10^4 MDs before gathering data. On average each simulation lasting 100×10^4 MDs was run on 48 processors for a total of 96 hours for each CPU. We run 3-5 independent simulations per parameter value.

C. The phase diagram

From extensive numerical simulations as the ones described above, and a systematic analysis of the pressure, correlation functions, local density and hexatic order distributions, we obtained the phase diagram of the hard ABP, with the potential defined in Eq. (2) [24]. A zoom over the high packing fraction part of it is presented in Fig. 1. The diagram includes a solid, a hexatic and a liquid phase, with the addition of the MIPS sector at sufficiently high Pe and a small co-existence region close to $\text{Pe} = 0$. The phase transitions are indicated with line-points (with different colors). We call ϕ_h the solid-hexatic transition density and ϕ_l the hexatic-liquid one. Note that for a first-order hexatic-liquid transition we denote by ϕ_l the high-density branch of the coexistence region. Clearly, both vary with Pe . The phase transition between liquid and hexatic, close to the passive limit, is of first order and it is accompanied by a narrow co-existence region which is shaded in blue in the figure. $\phi_{\text{cp}} \approx 0.91$ is the close packing fraction for hard disks. We refer to [24] for further details on how the MIPS, solid and hexatic regions were identified. On top of the latter “thermodynamic” transitions, in the present work we identify and characterize a novel geometric transition, associated with the percolation of clusters of defects, occurring at ϕ_P and represented in the phase diagram with red symbols.

Instrumental to measure orientational order, is the local hexatic order parameter

$$\psi_{6i} = \psi_6(\mathbf{r}_i) = \frac{1}{N_i} \sum_{k=1}^{N_i} e^{i6\theta_{ik}}, \quad (4)$$

with \mathbf{r}_i is the position of the i th disk and θ_{ik} the angle formed by the segment that connects its center and the one of its k th out of its N_i nearest neighbors, identified with a Voronoi construction. Pictorially, the local orientational order is represented with color maps in which the colors designate different projections of the local hexatic order on the orientation of the global hexatic order

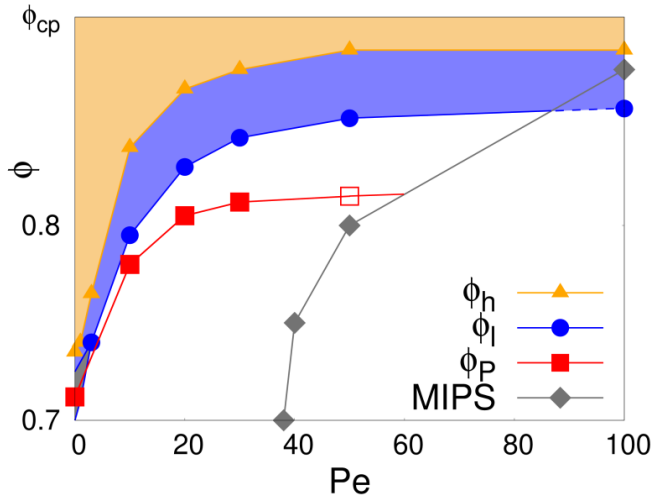


FIG. 1. Phase diagram of Active Brownian hard disks at high densities ($\phi > 0.7$). The blue line locates the hexatic-liquid transition, ϕ_l , which can either be discontinuous at low Pe (< 3 , opening up a coexistence region, shown in shaded gray), continuous at higher values of Pe , and even penetrate within the MIPS region (dashed line at high Pe). The orange curve is the solid-hexatic transition, ϕ_h , which is continuous for all values of Pe . The values of ϕ_h and ϕ_l at $Pe = 0, 10, 20, 30, 40, 50$ are given in Tables I and II, respectively. (For $Pe = 0$, ϕ_l is the upper limit of the coexistence sector.) The black curve delimits the coexistence region opened up by Motility-Induced Phase Separation (MIPS). The red curve indicates the percolation transition of (coarse-grained) clusters of defects occurring at ϕ_P . Filled red symbols are the ϕ_P extracted from the analysis of the probability of occurrence of a wrapping cluster, P^∞ , at different system sizes, while the empty one at $Pe = 50$ is determined from the inspection of the cluster size distributions, $P(n)$. The properties of this transition are largely discussed in Sec. VI. The close packing of hard disks sets the upper limit of the plot, at $\phi_{cp} \simeq 0.91$.

parameter of the system. This representation was used in several recent publications, see e.g. [22–24].

In this paper we also consider a soft disk system, see Eq. (3). The phase diagram is similar, although with the important difference that the transition between hexatic and liquid in the passive limit, and near it, is continuous (and not first order). In App. A we present the orientational correlation function in equilibrium at different packing fractions, and the equation of state (pressure against packing fraction) for soft disks. None of them shows evidence for a first order phase transition, in agreement with the previous report in [23] for a slightly different model.

III. TOPOLOGICAL DEFECTS

The topological defects are mis-coordinated particles, or cells in the Voronoi construction, with respect to the perfect hexagonal lattice, that is to say, the perfectly

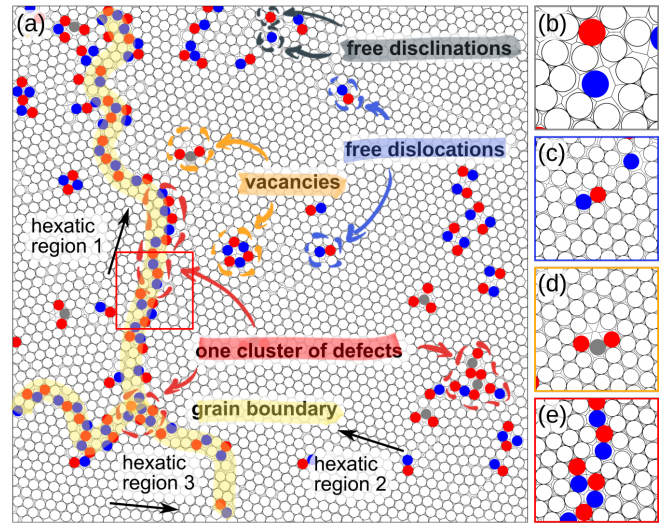


FIG. 2. (a) Detailed view of a typical snapshot ($\phi = 0.820$ and $Pe = 20$) with different kinds of defects. Particles in 5-fold cells are colored in red, 7-fold ones in blue, and all other mis-coordinated disks in gray. The large black arrows have the direction of the orientational order parameter in three regions of the system. Two disclinations are shown in (b), a dislocation and a disclination in (c), a vacancy in (d), and a detailed view of two clusters of defects belonging to the same grain boundary (shown in yellow in (a) and delimiting regions with different hexatic order) in (e).

ordered crystal. Free disclinations correspond to individual cells with 5 or 7 neighbors (5-fold and 7-fold defects), while free dislocations are pairs of neighboring cells with 5 and 7 neighbors (5-7 pairs). Vacancies are point defects resulting from the removal of a particle from the hexagonal packing, and can be identified with different configurations involving, either groups of pairs of bounded dislocations (two or more), or higher-order mis-coordinated cells (with less than 5 or more than 7 neighbors). All these localized topological defects might aggregate into clusters, giving rise to extended structures that we also identify and analyze.

The various types of defects can be seen in Fig. 2, where we plot a selection of a configuration of the active system at a rather high packing fraction. The four kinds of defects mentioned in the previous paragraph are zoomed over in the boxes next to the configuration in panel (a). We see two disclinations in (b), a dislocation in (c), a vacancy in (d), and a piece of two clusters of defects belonging to the same grain boundary in (e).

In this Section we explain the way in which we classified the defects (Subsec. III A), we define the number density of each defect kind and their radial correlation function (Subsec. III B), we describe the coarse-graining method used to build the clusters of defects (Subsec. III C), and we recall some elements of percolation theory that we will use later on (Subsec. III D).

A. Classification

The analysis of the defects was done according to the classification proposed by Pertsinidis & Ling in Ref. [72].

After having defined a defect core as a set of nearest-neighbor mis-coordinated particles, these authors point out that one configuration of defects can be said to come from a local rearrangement of particles around a vacancy if it satisfies the following properties:

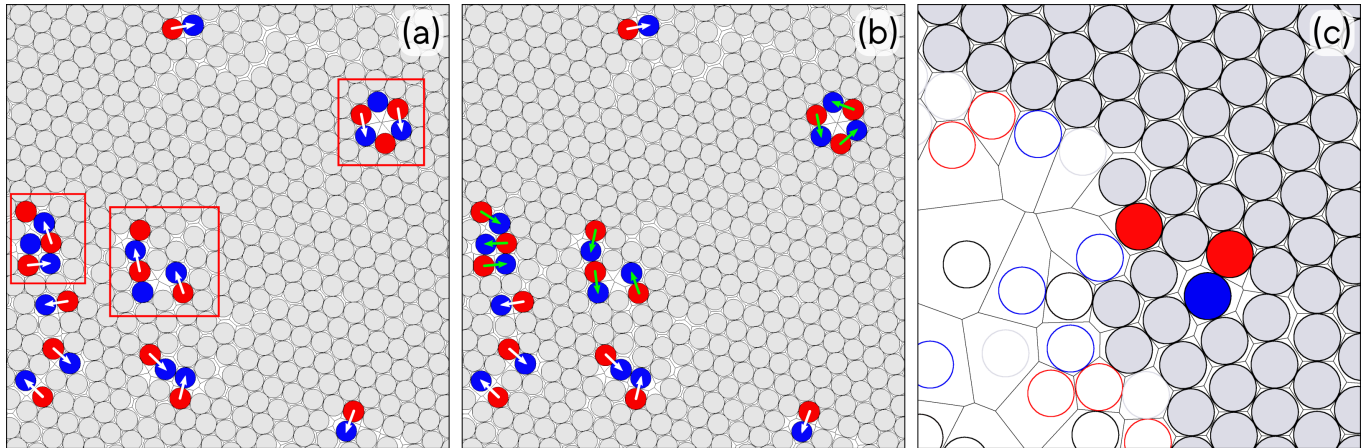


FIG. 3. Voronoi tessellation, with defected particles painted in blue (7 neighbors) and red (5 neighbors). The arrow assignment is explained in the text. We show here two cases: (a) Wrong assignment in the three red boxes. (b) Correct assignment for which an arrow is attributed to each pair of defected particles. Green arrows are the ones that changed from panel (a) and made the assignment correct. (c) Voronoi construction close to the boundary between the dense drop and the gas in the MIPS regime ($Pe = 200$ and $\phi = 0.890$). The filled gray disks belong to the dense phase and the empty ones to the gas. The empty disks which sit on defected Voronoi cells are not included in the counting of defects since they belong to the interface or to the gaseous phase.

- The mean coordination number is equal to six.
- The modulus S of the sum of vectors assigned as follows is equal to zero. Consider a set of unit vectors e_{ij} within the defect core, each one starting from a particle with coordination number $m_i < 6$ and ending in a nearest neighbor with coordination number $m_j > 6$. The vector \mathbf{S} is the sum of these vectors. This protocol is justified by noting that, for a single dislocation, the Burgers vector \mathbf{b} is in one-to-one correspondence to the vector defined above, being in particular \mathbf{b} equal to e_{ij} rotated counterclockwise by $2\pi/6$. Therefore, an arrangement of cells with vanishing S corresponds to a defect with zero Burgers vector.

Given the definition of a vacancy as a defect carrying zero Burgers vectors, all the other defects are classified in the following way.

- Free disclinations: one-particle defects.
- Free dislocations: a pair of nearest-neighbor 5-fold and 7-fold defected particles.
- Vacancies of size n : any configuration of n nearest-neighbor mis-coordinated particles with mean coordination number equal to six and $S < S_{th}$, where

S_{th} is a threshold value (replacing zero) taken to be a half of the mean separation between particles.

- A cluster of size n is any set of n nearest-neighbor mis-coordinated particles with $S > S_{th}$.

For large and complex groups of nearest-neighbor mis-coordinated Voronoi cells, there are many ways to arrange the vectors e_{ij} among all possible 5-7 pairs. One could attempt a complete enumeration that will eventually lead to the optimal assignment of vectors. Another option is to generate a large but not complete number of vector assignments and choose the best one among them, which is the one that accommodates the largest number of arrows, resulting in a maximally-covered configuration. We checked that this strategy is good enough to pinpoint the “maximally-covered” configuration for most of the defect groups. As two examples, Fig. 3 shows a “wrong” vector assignment in panel (a) and a “correct” one, which we will choose, in panel (b).

Finally, in panel (c), we zoom over the interface between the dense drop and the gas in a system with $Pe = 200$ and $\phi = 0.880$, within the MIPS coexistence region of the phase diagram (see App. B for the algorithm used to single out the dense particle cluster). We want to identify

defects within the dense phase only, and avoid counting the ones placed at the boundary between the two phases. For this reason, we spotted the particles or Voronoi cells at the interface and we excluded them from the statistics, see Fig. 3 (c). For example, in the snapshot shown, this led us to disregard from the counting the blue and red empty particles that are placed on defected cells but lie right on the boundary.

B. Number densities and correlations

We define the number density of defects, ρ_d , as the number of defected particles involved in all the defects of a given type (e.g., 2 for each dislocation) divided by N , the total number of particles,

$$\rho_d = \frac{1}{N} \# \text{ particles in the selected kind of defect} . \quad (5)$$

In two dimensions, the radial pair distribution function of any kind of point-like object is defined as

$$g(r) \equiv \frac{dn_r}{2\pi r dr \rho} . \quad (6)$$

Given the center of mass of such an object at the origin, $g(r)$ represents the probability of finding another one at distance r from it, relative to the one of an ideal gas. It therefore helps describing how the density of the objects under study varies as a function of distance from a reference one: dn_r is the number of items that are a distance between r and $r + dr$ away from the reference, and the denominator ensures normalization with respect to the angular average, with $2\pi r dr$ the area of a bidimensional spherical shell, and ρ the averaged number density. This ensures that $g(r) = 1$ when the system is structureless (for instance in the dilute or $r \rightarrow \infty$ limits).

C. Coarse-graining

Grain boundaries appear as chains of closely spaced defects (see Fig. 2), though the latter are not fully connected at the single Voronoi cell scale. We fill the microscopic gaps with a coarse-graining procedure routinely applied to study gelation [73]. The procedure is demonstrated in Fig. 4 with an example. The thin straight lines separate space into $d_x \times d_y$ rectangular cells, with different linear lengths d_x and d_y proportional to a length scale d_s . This choice guarantees the covering of the rectangular $L_x \times L_y$ simulation box. More concretely, we used $d_{x,y} = L_{x,y} / \text{int}(L_{x,y}/d_s)$, where int is the integer part function. A cell is painted yellow whenever the center of a defected particle lies within it. In this way a particle contributes to, at most, a single cell. Coarse-grained clusters of defects are built by joining together neighboring cells with at least one defect, that is, those painted yellow. Proceeding in this way, the microscopic

gaps are filled. We used this coarse-graining method in the analysis of the geometry and statistics of the defect clusters, focusing on the coarse-graining length $d_s = 3\sigma_d$. (A study of the effect of this parameter can be found in App. F.)

We typically found $\sim 10^4$ defected cells in each configuration in the hexatic phase, later not too close to the hexatic-liquid transition. Once classified in the different classes that we have just defined, we counted about 300 dislocations, 10 disclinations, 1000 vacancies (which on average include from 3 to 6 cells), and 100 clusters (of ~ 10 cells each). These numbers increase when we get closer to the hexatic-liquid transition. This gives an idea of the number of data points that we use in our statistical analysis.

Of interest for the geometrical characterization of the defect clusters, see Eq. (7), we identified the centers of mass of the clusters in the periodic box with the help of the method explained in Ref. [74].

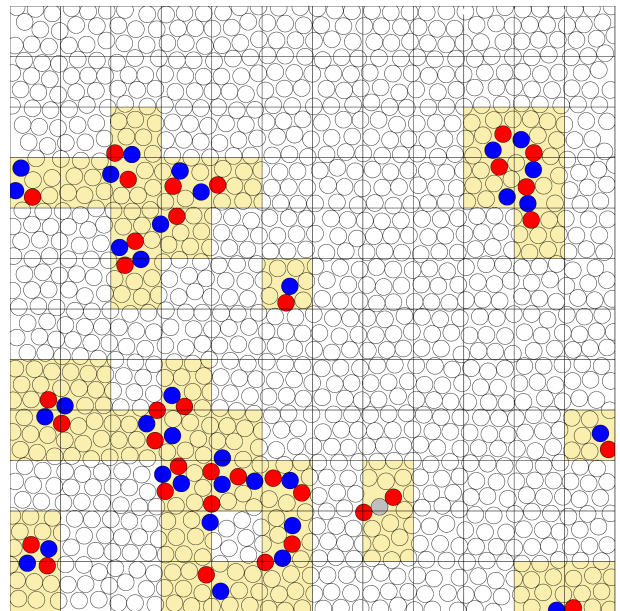


FIG. 4. Example of the coarse-graining procedure applied to the defect clusters with $d_s = 3\sigma_d$. Disks in red and blue are the particles with 5 and 7 neighbors in the Voronoi construction. Space is divided in rectangular cells painted yellow whenever the center of a defect particle falls in it. Coarse-grained clusters are built by joining such cells when they share a boundary.

D. Percolation

Percolation occurs when a connected cluster of defects wraps around the periodic boundaries of the system. In order to identify whether a cluster of defects is percolating we applied the method designed by Machta et al. [75, 76]. Accordingly, while running the algorithm to

organize defected cells into connected clusters, for each cluster we keep track of the paths connecting all the sites to the first defected cell we identified (i.e. the root of the algorithm). The wrapping condition for a given cluster is fulfilled whenever the difference between the paths (both along the x- and y-direction) of two different sites belonging to the cluster equals the system size.

Continuous percolation refers to the cases in which the concerned objects are placed in continuous space in contrast to the better understood lattice problem in which they occupy the sites of a regular structure. Percolation on a lattice is a specially appealing phenomenon since it is well understood theoretically and presents critical and universal features, with independence of the microscopic details [77]. In contrast, continuous percolation [78–80], as it arises, for example, in liquids, is not as well characterized analytically. Here, by mapping the continuous problem on a lattice one we get closer to the better understood discrete setting.

A way to locate the critical parameters for percolation in a system with periodic boundary conditions is to monitor the probability of occurrence of a wrapping cluster. Such probability is usually denoted P^∞ and, for finite size systems, it smoothly varies from 0 (no percolation) to 1 (complete percolation). P^∞ satisfies finite size scaling and, in the infinite size limit, it detaches from zero at the critical control parameter. The best way to estimate the latter in a finite size system is, therefore, to perform a finite-size scaling analysis: the curves $P^\infty(\phi)$ obtained for different sizes should cross at a common point, which we identify with the onset of percolation, ϕ_P .

Several characteristics of the clusters in a percolating problem have been defined and analyzed. An essential aspect of critical percolation is their fractal morphology. A way to study the clusters' geometry is to relate their size, n_C , giving the number of cells that constitute the cluster, to a length scale, e.g., their radius of gyration

$$R_{g_C} = \left[\frac{1}{n_C} \sum_{i \in C} (\mathbf{r}_i - \mathbf{r}_C)^2 \right]^{\frac{1}{2}}, \quad (7)$$

where the sum runs over all cells in the cluster and \mathbf{r}_C is the position of its center of mass. The relation between the size and gyration radius defines the fractal dimension d_f :

$$n_C \sim R_{g_C}^{d_f}. \quad (8)$$

Another key ingredient of percolation theory is the probability distribution function of cluster sizes, $P(n)$, which takes the form [77]

$$P(n) \simeq n^{-\tau_n} e^{-n/n^*}, \quad (9)$$

where the so-called Fisher exponent, τ_n , is related to the clusters' fractal dimension via

$$\tau_n = 1 + d/d_f, \quad (10)$$

and n^* diverges at the percolation critical point.

IV. THE KTHNY PICTURE: DEFECT UNBINDING

In the KTHNY picture, melting occurs in two steps, driven by the unbinding of dislocations and disclinations. Lowering the global packing fraction from a closed packed state, a first transition takes place when groups of four point-like defected particles, with five and seven neighbours in the Voronoi tessellation of space, separate in pairs of two. The latter are the so-called dislocations, which are formed by two connected particles with five and seven neighbours. Decreasing further the global packing fraction, a second transition takes place when dislocations dissociate into two isolated defected particles, or disclinations, which are then free to move within the full sample. This scenario is represented in Fig. 5.

The BKT-like transitions predict that the number density of free dislocations and disclinations, defined in Eq. (5), decay at the corresponding critical points ϕ_c as

$$\rho_d \sim a \exp \left\{ -b [\phi_c / (\phi_c - \phi)]^\nu \right\}, \quad (11)$$

with the parameters a and b and the critical packing fraction ϕ_c being non-universal, and the exponent ν taking the values

$$\nu \begin{cases} \simeq 0.37 & \text{at the solid-hexatic} \\ = 0.5 & \text{at the hexatic-liquid} \end{cases} \quad (12)$$

transitions. These are the results derived by Nelson & Halperin [12] and Young [13], following the development by Kosterlitz [81] for the 2DXY model.

In this Section we will study in depth the number density of dislocations and disclinations, and how they detach from zero at the solid-hexatic and hexatic-liquid transitions, putting special emphasis on the comparison to the predictions of the KTHNY theory. We complement this study with an analysis of the spatial organization of defects.

A. Number densities

We use the classification introduced in Sec. III A to identify the isolated dislocations and disclinations [72], namely, the isolated miscoordinated pairs of particles or single particles, respectively. In this analysis we associate them to free point-like defects. Unless otherwise stated, the data in the plots are sampled over 50 independent instantaneous configurations selected at sufficiently spaced times in the stationary regime.

The number densities of free dislocations and disclinations, see Eq. (5), are shown in Fig. 6 in four representative cases: (a) passive hard disks, $Pe = 0$; (b) ABP at $Pe = 10$; (c) ABP at $Pe = 20$; (d) ABP at $Pe = 100$. For equilibrium hard disks the liquid-hexatic transition is discontinuous, showing a coexistence region between the pure hexatic and liquid phases (gray area). In cases (b)

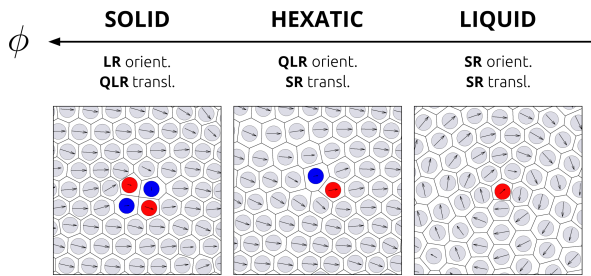


FIG. 5. Unbinding of dislocations and disclinations: the mechanism behind the solid-hexatic and hexatic-liquid phase transitions in the KTHNY theory. As in previous figures, disks in red and blue are 5-fold and 7-fold defected particles in the Voronoi construction. The arrows represent the local hexatic order parameter, see Eq. (4), attached to each particle and are used to quantify the bond orientational order. Close to the ϕ axis, the nature of the orientational and translational order characterizing the three phases are indicated: Long-Range (LR), Quasi-Long-Range (QLR) or Short-Range (SR).

and (c) the liquid-hexatic transition is continuous and (d) exhibits MIPS [24]. In the MIPS coexistence region we only count defects belonging to the dense phase. The values of the critical parameters separating solid, hexatic and liquid phase are taken from the analysis of the correlation functions and the equation of state presented in Ref. [24] for the hard disk model, see Tables I and II.

The first noticeable fact in all panels in Fig. 6 concerns the transition between the solid and hexatic phases. At the vicinity of the hexatic phase (blue background), the number of free dislocations increases sharply, indicating that they break positional QLRO and mediate the solid-hexatic transition at all Pe . This leads us to the following statement:

- The solid-hexatic transition in ABP interacting via a hard repulsive potential is consistent, at least qualitatively, with the KTHNY scenario.

Figure 6 also informs us about the dissociation of dislocations into disclinations close to the hexatic-liquid transition. The density of free disclinations (gray squares) is very close to zero in the hexatic phase and detaches significantly from this value when the liquid appears, either as a pure phase, in panels (b) and (c), or co-existing with the hexatic, in panels (a) and (d). We see that:

- The unbinding of disclinations arises in the liquid component of passive and active systems.

The data shown in Fig. 6 correspond to systems with $N = 512^2$ particles. We have performed a similar analysis in systems with less particles, e.g. $N = 256^2$, and found comparable results. For this range of particle numbers, we have not observed strong finite size effects. We argue why this is so when presenting a more specific data analysis of both dislocation and disclination number densities below. See also App. C.

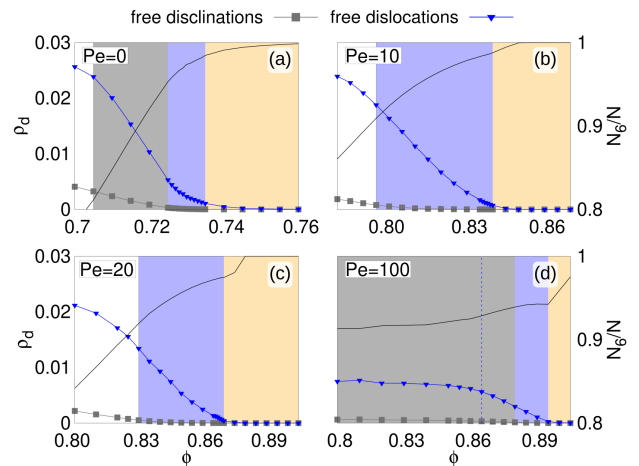


FIG. 6. Number densities of isolated disclinations and dislocations as a function of ϕ for passive hard disks (a), ABP at $Pe = 10$ (b), ABP at $Pe = 20$ (c) and ABP at $Pe = 100$ (d). Black solid lines represent the number density of non-defected particles, following the scale on the right vertical axis. We will discuss the nature of the defected particles which are not dislocations or disclinations in Secs. V and VI. The solid, hexatic, phase-coexistence and liquid regions are shown in orange, blue, gray and white backgrounds, respectively. The values of the critical parameters separating solid, hexatic and liquid phase are taken from the analysis of the correlation functions and the equation of state presented in Ref. [24] and recalled in Tables I and II. The dashed blue vertical line inside the MIPS region (d) indicates the ϕ above which local orientational correlations are scale-free. All quantities are obtained after averaging over $\simeq 50$ independent configurations sampled from 3 independent simulations. See Sec. III B for the typical number of defects observed in each independent run.

In Fig. 6 we also plot, with thin black lines, the % of non-defected particles, that is to say, those which are 6-fold connected, with the scale given in the right vertical axis. Note that, as in Ref. [82, 83], there is quite a lot of 6-fold order even in the liquid phase, not too far from the hexatic-liquid transition, with approximately 80% of the particles being of this kind.

B. Solid-hexatic transition: dislocations

A precise quantitative analysis of the way in which the density of free dislocations departs from zero at the solid-hexatic transition is notably hard even in the passive case. For example, the curves for the free dislocation density shown in Fig. 3a in [25] are not accompanied by a fit. Still, we have performed a convincing analysis of our data points, which exhibit the behaviour predicted by the BKT singularity.

We fit the free dislocation number densities shown in Fig. 7 using Eq. (11) close to the solid-hexatic transition for various values of the Péclet number. The fits were performed over the data in the hexatic and solid phases

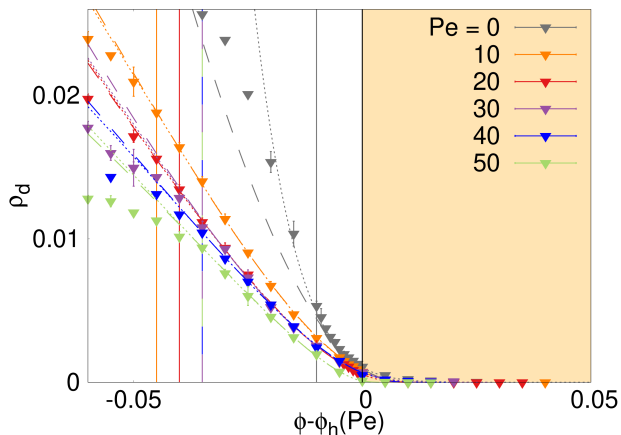


FIG. 7. Number density of dislocations close to the solid-hexatic transition at different Pe given in the key. The values of the off-set $\phi_h(\text{Pe})$ in the horizontal axis are the ones found with the methods in [24], recalled in Table I. The region painted orange corresponds to the solid phase. Dotted and broken lines show three (a, b, ϕ_c) and four (also ν) parameter fits, respectively, to the form in Eq. (11). In one fit the exponent is fixed to the KTHNY value $\nu = 0.37$ and the values of the fitting parameters and the χ^2/ndf are reported in Table I. In the other fit ν is also an adjustable parameter, see App. E for details. All fits are performed over the data in the hexatic and solid phases only, delimited by the vertical dashed lines to the left of the origin (of different color for each Pe).

only: the fitting intervals for the different Pe values are delimited with vertical color lines. For all Pe the fitted curves deviate from the data as soon as these cross the hexatic-liquid transition.

Equation (11) has four parameters and we followed different fitting procedures to determine them. We first fixed the value of the exponent ν to the one predicted by the KTHNY theory in the passive limit, $\nu = 0.37$ [12, 13], leaving ϕ_c , a and b as fitting parameters. In App. D we give more details on this fitting procedure and we estimate the confidence interval of the parameters a and b . Alternatively, we considered ν as a fourth adjustable parameter, see App. E. We present the analysis as a function of $\phi - \phi_h(\text{Pe})$ with $\phi_h(\text{Pe})$ the solid-hexatic transition value obtained from the study of correlation functions and local probability densities [24].

Although the performance of the two fitting procedures may seem similar, a better judgement of their relative quality is gained from the comparison of the fitted $\phi_c(\text{Pe})$ and $\phi_h(\text{Pe})$, see Table I and App. E (a similar strategy was applied to the 2DXY model in [84]). The two values are closer when the exponent ν is fixed to $\nu = 0.37$, the HNY value. The fitted values of ϕ_c at different Pe are around 1-2% off the ones determined with the measurements of correlation functions and probability density profiles [24], providing an alternative way to locate the solid-hexatic transition. Indeed, in our ABP model ϕ_c is only slightly above ϕ_h in the five active cases con-

Pe	ν	a	b	ϕ_c	ϕ_h	χ^2/ndf
0	0.37	8	2	0.75	0.735	1.61
10	0.37	1.5	1.61	0.853	0.840	2.76
20	0.37	1.2	1.59	0.883	0.870	1.34
30	0.37	2	1.9	0.897	0.880	2.08
40	0.37	0.81	1.47	0.898	0.885	0.791
50	0.37	0.38	1.17	0.895	0.890	0.493

TABLE I. Dislocation unbinding at the solid-hexatic transition. Analysis of the fitting parameters in Eq. (11) for the density of free dislocations plotted in Fig. 7. The exponent is fixed to the HNY value, $\nu = 0.37$. The values of $\phi_h(\text{Pe})$ are the ones estimated from the analysis of the correlation functions and probability densities in [24], while $\phi_c(\text{Pe})$ are extracted from the fit.

sidered when $\nu = 0.37$ (e.g. $\phi_c = 0.853$ vs. $\phi_h = 0.840$ at $\text{Pe} = 10$). A similar weak deviation between the critical points was measured by Han et al. [85] in their experiments with a passive microgel. We note, however, that close to ϕ_h , these authors found around 10 times more dislocations than we do. Far from ϕ_h the percentage of dislocations in [85] and here are similar. The different form of the fitting curve in [85] compared to ours is due to the excess in $\rho_d(\phi_h)$. The increase around ϕ_c is controlled by the parameter b in the fitting curve, which should take a larger value in [85] (not reported) than in our fit. The proportion of particles in dislocations and the form of the curve ρ_d are similar to ours in other simulations, see e.g. [25, 86], though no quantitative analysis of the critical behavior was performed in these references.

One may wonder how robust the results in Table I are against coarse-graining. The coarse-graining procedure explained in Sec. III C builds aggregates, like the ones shown in Fig. 4, by gathering together the single defects that are closer than the coarse-graining length d_s . After this construction, one computes the number density of all defect species with the classification scheme of Sec. III A. Quite naturally, the number of dislocations and disclinations is diminished after coarse-graining since many of them get attached to larger clusters. In App. F, see Fig. 31, we study the effect of the coarse-graining length d_s on the critical behaviour of the number density of dislocations close to ϕ_h . The three parameter fit, with fixed $\nu = 0.37$, yields values of ϕ_c that steadily approach (from above) the ϕ_h measured in [24] for d_s increasing from 2 to 5. (In studies of the vortex pair unbinding at the BKT transition of quantum gases, the filtering induced via coarse-graining also has the effect of approaching the vortex unbinding temperature to the critical one [87].)

We conclude that the dislocation data are consistent with the HNY exponent $\nu = 0.37$ all along the solid-hexatic transition, and we therefore state that:

- The solid-hexatic transition in ABP interacting via a hard repulsive potential complies with the KTHNY scenario even quantitatively. Our measurements suggest that the exponent ν is independent of Pe on this critical line.

An example of a typical configuration in the hexatic phase with several dislocations is displayed in Fig. 9(b). One can appreciate the spatial arrangement of dislocations which will be analyzed in Sec. IV D.

C. Hexatic-liquid transition: disclinations

In the KTHNY scenario the hexatic-liquid transition is driven by the dissociation of dislocations into free disclinations. We now investigate whether this is indeed what occurs for passive and active Brownian disk systems.

Figure 8 displays KTHNY fits, Eq. (11), to the number density of disclinations close to the packing fraction where they detach from zero. We follow the procedure already used to analyze dislocations, and consider both a protocol where ν is fixed to its expected theoretical value $1/2$, see also App. D, and an alternative approach where ν is a fourth fitting parameter. We compare the quality of these fits according to two criteria: how the critical $\phi_c(\text{Pe})$ extracted compares to the ϕ_l previously determined [24], and whether the values of the fitting exponent are reasonable.

Concerning ϕ_c we see that the values found with the four-parameter fit are higher and possibly too close to the ϕ_h of the solid-hexatic transition, see Table V in App. E. Nonetheless, this is not enough to exclude this fit since, all in all, the distance between the fitted ϕ_c and the critical values estimated in [24] are similar in the two protocols, see Table II.

The second test, that is, whether the values of the fitted ν follow a reasonable trend as a function of Pe , suggests, though, that the four parameter fit is less reliable: the fitted ν reported in Table V varies strongly and in a non-monotonic way with Pe and, moreover, for some Pe takes unreasonable values. Therefore, one would conclude that the three-parameter fit with $\nu = 0.5$ is more consistent and quite satisfactory.

Nevertheless, going back to Fig. 8 and looking at the raw data one notices that the trend of the curves, organized from top to bottom as Pe increases from 0 to 30, is inverted for larger Pe . Moreover, the density of disclinations for $\phi > \phi_l(\text{Pe})$ is considerably larger than zero at high Pe , which obscures the interpretation of the data and the subsequent fits.

A better understanding of what happens close to the hexatic-liquid transition is gained from the visualization of the local hexatic order parameter, Eq. (4), and the defects configurations. An example is shown in Fig. 9 for parameters such that the system is in the hexatic phase, above but close to $\phi_l(\text{Pe})$, where a few disclinations yield a non-vanishing (but small) ρ_d . The first observation is that disclinations are not free to move apart: they are very close to ensembles of many defects. This can be appreciated in panel (b), where two gray circles highlight two defected particles that count as free disclinations. These disclinations are located in regions where the local hexatic order deviates from the majority (red) orienta-

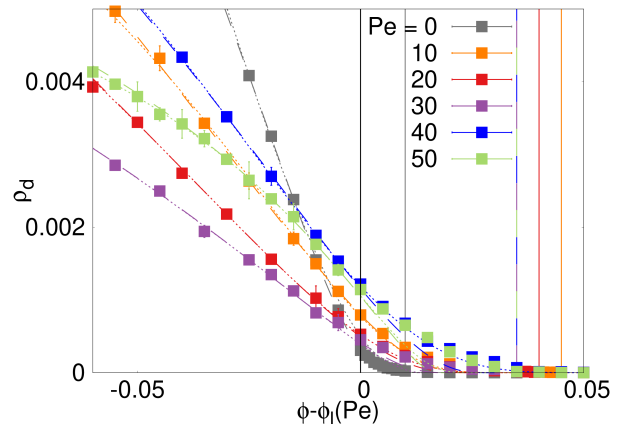


FIG. 8. Number density of disclinations close to the hexatic-liquid transition at different Pe . The values of the off-set $\phi_l(\text{Pe})$ in the horizontal axis are the ones in Table II. Dotted and broken lines show three (a, b, ϕ_c) and four (also ν) parameter fits, respectively, to the form in Eq. (11). In Table II we give the values of $a, b, \phi_c, \phi_l(\text{Pe})$ and the χ^2/ndf for the three parameter fit. Details on the four parameter fits are given in App. E. All fits are performed over the data in the liquid phase only. Colored vertical lines show the location of the solid-hexatic transitions $\phi_h(\text{Pe})$ for all the Pe values considered.

tion, see Fig. 9 (a). On top, these disclinations cannot freely move around and they do not destroy the quasi-long-range orientational order of the hexatic phase. Finally, the local character of these point-like defects also explains why we do not see strong finite size effects in the measurement of ρ_d in this range of parameters: there is no characteristic length associated to them which could be in competition with the linear system size (see App. C). More generally, Fig. 9 demonstrates that close to the hexatic-liquid transition defects are not just point-like: they aggregate forming large objects that invade the sample in a way that we discuss in Sec. VI.

In App. F, see Fig. 32, we show the results of counting

Pe	ν	a	b	ϕ_c	ϕ_l	χ^2/ndf
0	0.5	0.072	0.62	0.734	0.725	0.430
10	0.5	0.06	0.81	0.823	0.795	1.09
20	0.5	0.05	0.8	0.857	0.830	0.710
30	0.5	0.025	0.64	0.866	0.845	0.895
40	0.5	0.053	0.71	0.880	0.850	0.809
50	0.5	0.016	0.41	0.874	0.855	0.233

TABLE II. Disclination unbinding at the hexatic-liquid transition. Analysis of the fitting parameters in Eq. (11) for the density of disclinations plotted in Fig. 8. The exponent ν is fixed to the KTHNY value $\nu = 0.5$. The values of $\phi_l(\text{Pe})$ are the ones estimated from the analysis of the correlation functions and probability densities in [24], while $\phi_c(\text{Pe})$ are extracted from the fit. At $\text{Pe} = 0$, ϕ_l is the upper limit of the co-existence region.

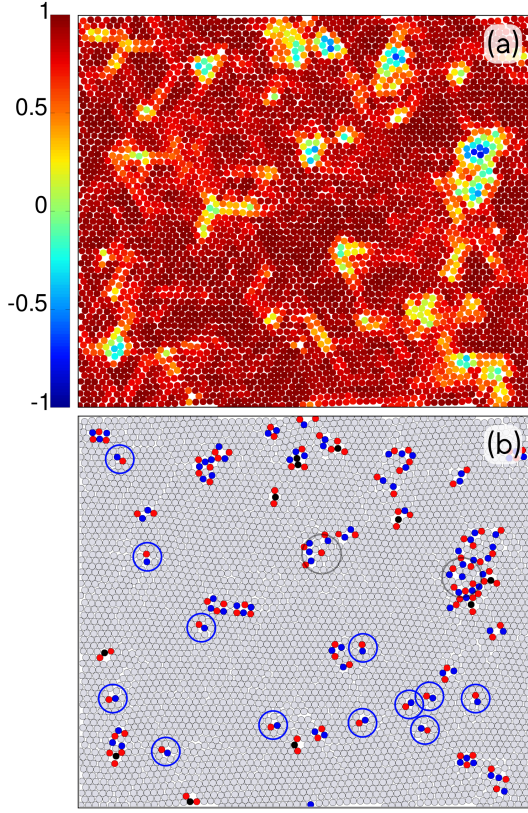


FIG. 9. Local hexatic order and defects for $\phi = 0.805$ and $Pe = 10$. Since $\phi_l = 0.795$ and $\phi_h = 0.840$ at $Pe = 10$, the case shown lies within the hexatic phase, close to the melting transition. (a) Each disk is colored according to the projection of the local hexatic order parameter (4) along the horizontal axis. (b) The defected particles in the same configuration are shown in red and blue. Blue and gray circles enclose dislocations and disclinations, respectively.

the number of disclinations after applying the coarse-graining procedure explained above, Sec. III C. Contrary to what happened with the dislocations, as soon as $d_s \geq 3$ we remove practically all disclinations and end up with an almost vanishing associated number density. The analysis of the pair correlation of disclinations in Subsec. IV D gives further support to their spatial proximity to other defects and to the fact that they can be erased by an even mild coarse-graining.

In conclusion, the behavior of the disclination number density close to the hexatic-liquid transition is more complex than the one of dislocations at the solid-hexatic threshold.

- The analysis of the number density of disclinations is not incompatible with the KTHNY fits with $\nu = 0.5$. However, the proximity of the solid-hexatic transition interferes with the analysis of the hexatic-liquid one. More importantly, other features conspire against the simple unbinding interpretation. Disclinations do not appear to be free but are notably close to large defected structures. This suggests that some other mechanism may also be at work at the hexatic-liquid transition.

D. Radial distributions: spatial organization

We analyze the spatial organization of particles, dislocations and disclinations by measuring their spatial correlation functions defined in Eq. (6).

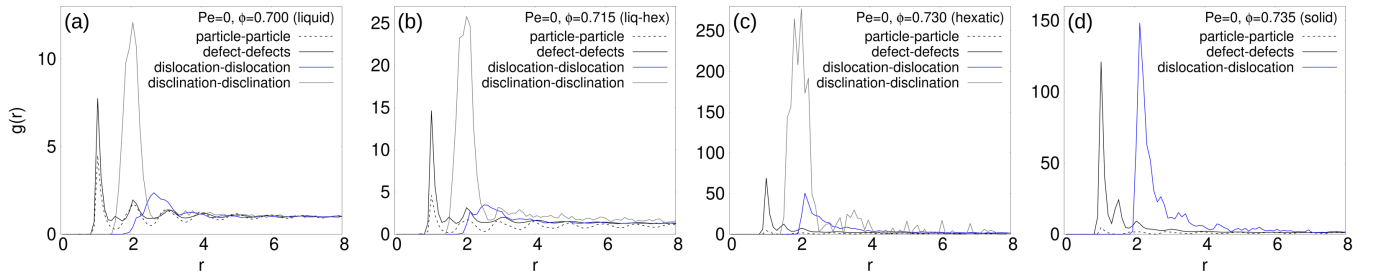


FIG. 10. Radial distribution functions defined in Eq. (5) in the various equilibrium phases. The curves represent the data for all particles (dashed black), all defected particles (solid black), dislocations (blue), and disclinations (gray). The global packing fraction increases from left to right and is indicated in the keys together with the corresponding phases are indicated in the keys. In the solid phase, panel (d), disclinations are absent.

The radial distribution function for different species is shown in Fig. 10 for passive systems in the liquid, co-existence region, hexatic and solid phases. The

peak structure of the particle-particle radial distribution (dashed curves) reproduces the well-known behavior of a hard-disk system at the value of surface fraction con-

sidered [88, 89]. The location of the peaks in the defect pair correlation is very close to the one of the particles themselves because defected particles are immersed in the dense disks layer. Therefore, except for small fluctuations in their position, they copy the same underlying structure of the whole sample. The dislocation-dislocation radial distribution function (blue curves) has a relatively wide bump departing from zero at $r \approx 2$ and centered at distances $r \approx 3$. It represents the probability density of separation between dislocations, like the ones highlighted in Fig. 9.

The disclination $g(r)$ presents a first peak at $r \approx 2$ which is much more pronounced in the hexatic and solid than in the liquid. This supports the expectation that point-like defects are more tightly bonded in the ordered phases. Still,

- the isolated disclinations are likely to stay close to each other even in the liquid, where one would have expected them (accordingly to the KTHNY scenario) to separate the most.

This is confirmed by the fact that, upon coarse-graining, the number of disclinations drastically diminishes when using a coarse-graining length larger than $r = 2$, see App. F. These features are similar to the results reported for the Gross-Pitaevskii classical field equation for Bose gases, in which positive and negative vortices show a pairing correlation that does not disappear above T_{KT} [87].

The conclusion is that

- dislocations do not pack as closely as disclinations do; they have more freedom, with the consequence of broadening the first peak of their $g(r)$.

This conclusion is consistent with the analysis of number densities of dislocations and disclinations, reported in Figs. 7 and 8. The number of dislocations grows in agreement with the KTHNY theory at the vicinity of the solid-hexatic transition, while the analysis of disclinations close to the hexatic-liquid transition is less conclusive. As we will see in Sec VI, extended structures of topological defects are the key objects allowing to further characterize the hexatic-liquid transition.

Let us now turn to the active case. Figure 11 shows the $g(r)$ of dislocations (a) and disclinations (b) at $Pe = 10$, and for different densities across melting. As the density increases, as expected, the spatial organization of dislocations gets magnified because the overall number of defects decreases. Moreover, the denser the system, the sharper the first peak located at a distance $r \approx 3$ (as in equilibrium), with respect to the others. For disclinations, on the contrary, there is not much change in the form of $g(r)$ while increasing ϕ from the liquid to the hexatic. We show only one case in the hexatic phase, $\phi = 0.795$, very close to the critical point, in order to reveal the behavior of residual tightly bonded disclinations in the ordered phase. Furthermore, we observe that the

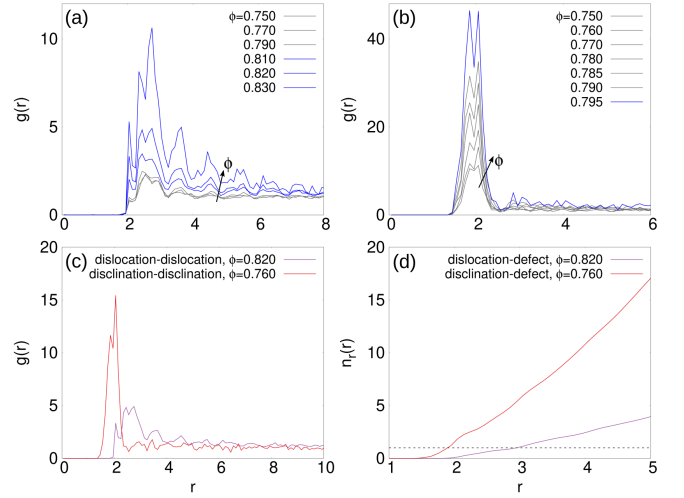


FIG. 11. Radial distribution functions of dislocations (a) and disclinations (b) at $Pe = 10$, and the packing fractions given in the keys. Blue curves are in the hexatic and black in the liquid phase. The normalization of $g(r)$ with the density of defects contributes to the growth of the first peak for higher ϕ . (c) Radial distribution functions at $Pe = 10$ for dislocations at $\phi = 0.820$ (hexatic phase, violet curve) and disclinations at $\phi = 0.760$ (liquid phase, red curve). The surface fractions were chosen so that dislocations and disclinations have a similar number density, $\rho_d \approx 0.003$. (d) Average number of defected particles at a distance r of a dislocation (red curve) and disclination (violet curve) for the ϕ 's in the key.

first peak develops a fine structure, composed of two sub-peaks evidenced in Fig. 11 (b). Such fine structure is also present in equilibrium, as shown in Fig. 10 (c). Figure 12 illustrates the local configurations that give rise to the double first peak. The disclinations are separated by one

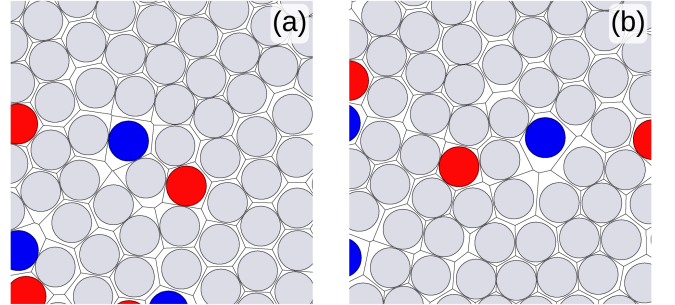


FIG. 12. Configurations at $Pe = 10$ and $\phi = 0.75$ with two nearby disclinations. A segment joining the centers of the two defected particles is almost perfectly aligned with the boundary of a Voronoi cell in (a) and it crosses two boundaries of Voronoi cells in (b). The length of the segment is very similar in the two panels, but not identical, and such difference gives rise to the two sub-peaks in the disclination-disclination $g(r)$, around $r \approx 2$, see Fig. 11 (b).

single lattice layer, while the ones belonging to the second sub-peak have one dislocated lattice layer in between. The difference between the two configurations can also be

understood from the inspection of the Voronoi tessellation close to the defected particles, see the caption of Fig. 12 for more details. We clarify the difference between the pair distribution of dislocations and disclinations with a direct comparison in Fig. 11 (c) of two cases where the number density of the two species are similar. While for dislocations we have $g(r) > 1$ over a significant extent beyond $r \approx 2$, for disclinations the distance probability density is extremely concentrated around the minimum value $r \approx 2$. In addition, the total number of defects of any species at a distance r , n_r , grows much faster for disclinations than for dislocations. Moreover, for disclination, it reaches $n_r = 1$ at $r \approx 2$ (see Fig. 11 (d)), further confirming that, even deep in the liquid phase, every disclination has on average one neighboring defected particle at a distance smaller than 2.

V. MIPS AND FINITE LENGTH STRINGS

In this Section we focus on parameters in the MIPS region of the phase diagram (for some recent studies of this phase see [90–94]) where the system separates into a macroscopic dense and a dilute phase, and we investigate the defects in the dense component only. In other words, we do not consider the particles in the dilute phase nor in the bubbles within the dense one [95], even though they are most likely mis-coordinated. For the same reason, we do not count the particles sitting on the boundaries between the dense phase (see App. B for the method used for its identification) and the gas, see Fig. 3.

In short, we start by evaluating the number density of point-like defects and we then study more complex structures made by nearby topological defects. We will find an extended, though finite-length, network of defects which separates orientationally ordered micro-domains [95].

A. Point-like defects

The parameter dependence of the number density of point-like defects across the MIPS coexistence sector is displayed in Fig. 13. The number density of each kind of defect remains practically constant below the packing fraction that we identified as the end of the QLR hexatic order [24] and until the low density spinodal [24, 96]. Therefore,

- the bulk of the dense phase generated through MIPS is characterized by a density of point-like defects set by Pe and not ϕ .

This is another aspect of MIPS that behaves as in equilibrium phase-separation: in the NVT ensemble, the parameter that triggers the phase separation, here Pe (would be the temperature T in an equilibrium system of attractive particles), controls the nature of the two co-existing phases, hence the density of point-like defects,

while the mean particle density sets the fraction of the system belonging to each of them.

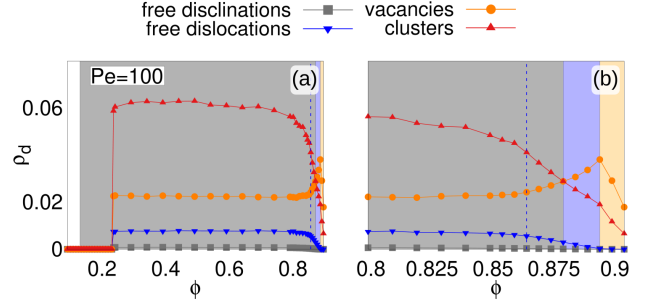


FIG. 13. Number density of all kinds of defects at a fixed high Pe and varying ϕ . The gray zone is the MIPS sector of the phase diagram and the dashed blue line inside it indicates the ϕ above which local orientational correlations are scale-free. Panel (b) zooms over the high ϕ region. The number density of vacancies has a net peak at the solid-hexatic transition. The decrease in number to the left of the peak is concomitant with the increase in dislocation number. The number density of vacancies is ϕ independent in MIPS below the hexatic dotted line. The same conclusion applies to the density of defected particles in clusters.

Besides dislocations and disclinations, vacancies are another kind of localized defect that displays an interesting parameter dependence within MIPS. In the way we defined them, vacancies include bounded dislocation pairs [72], they do not break positional QLRO, and can thus be present in the solid phase. As shown in Fig. 13, the number of vacancies increases as the density is decreased in the solid regime, but rapidly decays as we get into the hexatic phase, leaving a peak at the transition. Such decay is concomitant with an increase in the number of dislocations, since some vacancies can be thought of as two bounded dislocations. Besides a high ϕ region, where the solid and hexatic phases penetrate MIPS, the number density of vacancies also remains constant within MIPS.

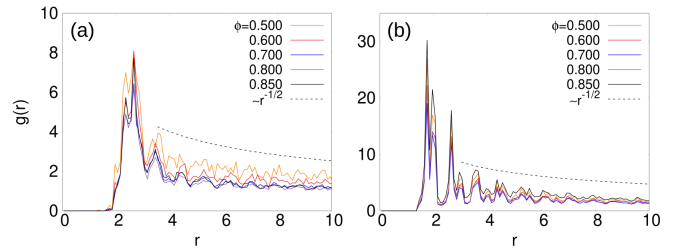


FIG. 14. Variation with ϕ of the radial distribution functions of dislocations (a) and disclinations (b) in the MIPS phase of the active system at $Pe = 100$. The quasi-periodic peaks in both panels have an envelope which falls off algebraically and is well represented by $r^{-1/2}$.

Figure 14 displays the pair correlation of dislocations and disclinations in the dense phase of MIPS at different

global packing fractions. The curves have multiple well-defined peaks with decreasing height at farther distances, and they remain almost unchanged when varying ϕ . This is again consistent with the fact that the actual density of the dense phase is set, approximately, by the upper limit of MIPS and is hence independent of ϕ . The spatial distribution of disclinations displays a sharper peak structure, indicating that disclinations are more correlated in space than dislocations, forming a structure with a higher degree of order. Note that the two sub-peak structure of the disclination $g(r)$ at very short r , already reported in Fig. 11, is also present in MIPS. Finally, compared to the correlations in the passive system or for weak activity, there are many more sharp peaks here. Interestingly enough, these peaks have an envelope that is well approximated by the algebraic decay $r^{-1/2}$. This decay is much slower than what we saw in homogeneous phases and we will argue that it is due to the string-like organization of defects in the dense phase built via MIPS that we discuss below.

B. A network of defects

Up to now we have focused on point-like defects: dislocations, disclinations and vacancies. However, most mis-coordinated particles in the MIPS dense phase cannot be identified as such, but appear in clusters comprising several defected particles.

Figure 13 also shows (with red triangles joined by lines) the number density of particles belonging to clusters of topological defects. Apart from a relatively sharp increase close to the upper limit of the MIPS region, this curve is approximately ϕ independent all the way until the lower (spinodal) limit of MIPS.

The structure of these clusters can be appreciated in the image in Fig. 15. We show in (a) the local hexatic order color map with finite-size hexatic domains. The right panel (b) displays the same configuration with 6-fold coordinated particles painted in gray, the ones with 5 neighbors in red, those with 7 neighbors in blue, and the ones with less than 5 or more than 7 neighbors in black. The particles in the gaseous phase are eliminated and do not appear in the image. An enlargement of the zone within the rectangle is displayed in (c), and demonstrates a nearly linear arrangement of defects along an interface.

The analysis in [95] showed that the MIPS dense phase is a patchwork of micro domains with different orientational order separated by rather sharp interfaces. In stationary conditions their radii \tilde{R}_H are exponentially distributed according to

$$P(\tilde{R}_H) \simeq R_H^{-1} e^{-\tilde{R}_H/R_H}. \quad (13)$$

The characteristic length-scale R_H coincides with the averaged one, $\langle \tilde{R}_H \rangle = \int d\tilde{R}_H \tilde{R}_H P(\tilde{R}_H)$, and it follows $R_H \simeq \ln(\text{Pe} - a) + b$ as estimated from a two parameter (a, b) fit, see the inset in Fig. 4 (b) in [95]. R_H is

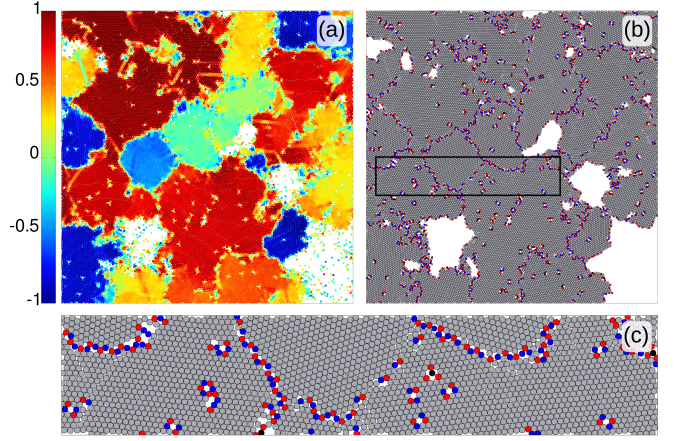


FIG. 15. A zoom over a region of the dense phase in the MIPS regime. (a) The map of the local hexatic order parameter projected on the horizontal direction. (b) Defects represented in red (particles with 5 neighbors) and blue (particles with 7 neighbors) in the background of 6-fold coordinated particles (in gray) and the gas (in white). (c) Enlargement of the zone surrounded by a rectangle in (b).

weakly dependent on ϕ . As the hexatic micro-domains are compact, from R_H one can estimate an averaged hexatic area, $A_H = \pi R_H^2$. The values taken by $A_H = \langle \tilde{A}_H \rangle$ at three Pe values are given in Table III.

The dense phase is also populated by gas bubbles [95, 97] with algebraically distributed radii

$$P(\tilde{R}_B) \simeq \tilde{R}_B^{-\tau_B} e^{-\tilde{R}_B/R_B^*} \quad (14)$$

with a Pe-independent exponent $\tau_B \simeq 2.2$ and R_B^* increasing with Pe [95]. The exponent τ_B is also independent of ϕ , at least at high ϕ where the bubble statistics can be reasonably well sampled. The lower the packing fraction, the larger the cutoff R_B^* , since the total gas-phase increases and a few bigger bubbles appear [98]. In Table III we also report the mean area of the bubbles, $\langle \tilde{A}_B \rangle$, for the same three Pe values.

The enlargement of the dense component in Fig. 15, with the hexatic domains and gas bubbles, illustrates the features just described. The configurations are smooth in the sense that the areas of both hexatically ordered patches and gas bubbles are not fractal but rather scale as $\tilde{A}_H \propto \tilde{R}_H^d$ and $\tilde{A}_B \propto \tilde{R}_B^d$ with $d = 2$.

The crossover between the averaged area of the hexatically ordered patches and the bubble size from $\langle \tilde{A}_H \rangle < \langle \tilde{A}_B \rangle$ to $\langle \tilde{A}_H \rangle > \langle \tilde{A}_B \rangle$ as Pe increases reported in Table III, can also be appreciated in the snapshots in Fig. 18. These two scales, $\langle \tilde{A}_H \rangle$ and $\langle \tilde{A}_B \rangle$, are shown as red (hexatic) and black (bubbles) filled disks above the first row.

The dense phase formed via MIPS is thus plagued with defects forming elongated clusters, or strings, associated to the formation of grain boundaries delimiting regions with different orientation. One can also clearly see from Fig. 15 that the defect strings tend to form a network but are also interrupted by the gas bubbles in cavita-

tion [95, 97]. These chains of closely spaced defects are not fully connected at the single cell scale, as evidenced in Figs. 2 (e) and 15 (b). We therefore treated the configurations with the coarse-graining procedure explained in Sec. III C with $d_s = 3\sigma_d$. Clusters of defects obtained with this technique are shown in Fig. 18. (The boundaries with the gas bubbles are also occupied by defected particles but we recall that we do not count them.) All in all, we identified in this way the coarse-grained clusters of defects that we next analyze with the tools devised to understand the morphology and statistics of percolating objects, recalled in Sec. III D.

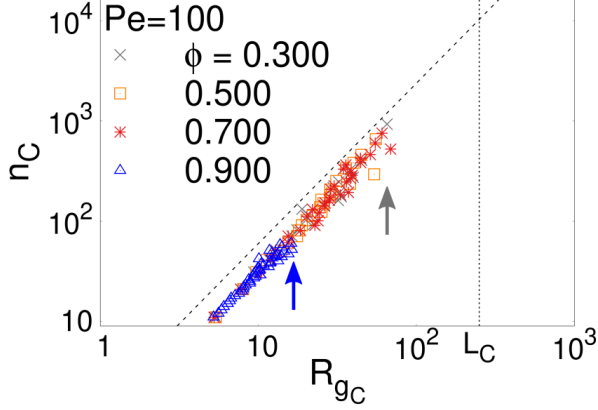


FIG. 16. Scatter plot of the size of the defect clusters against their radius of gyration for parameters at high activity, in the MIPS region of the phase diagram. The blue and gray vertical arrows point towards the largest n_C for ϕ in the hexatic phase and in MIPS, respectively. From $n_C \simeq R_{gC}^{d_f}$, shown with a dashed line close to the data, the estimated fractal dimension is $d_f = 1.60$ (error bars are given in Table III). The vertical dotted line indicates the approximate linear size of the dense droplet in MIPS (for a system with equal area of dense and gaseous phases for which $L/2 \approx 250$).

A measure of the length scale of a cluster is given by its radius of gyration R_g . The data in Fig. 16 are scatter plots for the cluster size, n_C , against the radius of gyration, R_{gC} , in systems with different packing fraction but all at the same $Pe = 100$. Again, within our numerical accuracy, all data fall on top of each other yielding a single estimate for the fractal dimension $d_f \simeq 1.60$. The error bars for this measurement and the ones at other Pe are given in Table III. Data for other Pe values also show ϕ independence (within our numerical accuracy). The outcome of the evaluation of d_f are reported in Table III, see also the gray data-points in Fig. 24. The results show a monotonic weak decay with Pe varying, roughly, from 1.65 at $Pe = 50$ to 1.57 at $Pe = 200$. In short, we see

- a weak decay of d_f with increasing Pe , which suggests that the cluster network gets thinner as Pe increases.

The cluster size distribution $P(n)$ is shown in Fig. 17. It was obtained by counting the number of coarse-grained

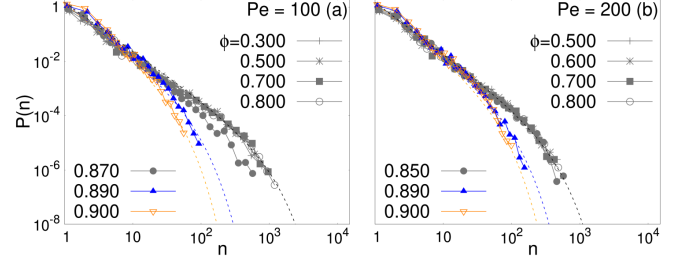


FIG. 17. Probability distribution of defect cluster sizes at $Pe = 100$ (a) and $Pe = 200$ (b) and several packing fractions, across the different phases. The data represented in gray lie in the MIPS region, while the blue and orange in the hexatic and solid, respectively. The outlier gray data in (a) are for parameter within MIPS, in between the lower limit of the hexatic phase and the end of MIPS. Decays of the type $n^{-\tau_n} e^{-n/n^*}$ with $\tau_n \simeq 2.2$ are shown with dotted lines ($n^* \simeq 30$ in the solid, $n^* \simeq 50$ in the hexatic for $Pe = 100$ and $Pe = 200$ alike, $n^* \simeq 500$ for $Pe = 100$ and $n^* \simeq 200$ for $Pe = 200$ in the MIPS region). The data in the MIPS phase with hexatic order are compatible with the 2.2 exponent, though with a shorter cut-off than the rest. This is due to the presence of a macroscopic single-color hexatic domain (implying the divergent hexatic correlation length) and small regions of others colors. Thus, the domain boundaries are also shorter.

clusters made of n defected cells at $Pe = 100, 200$ and various values of ϕ specified in the keys. The data in the solid (orange) and hexatic (blue) are separated from all curves within the MIPS region of the phase diagram (gray), that fall on each other (apart from one outlier which is in the hexatic region within MIPS). Thus,

- the defect cluster size distribution and the morphology of the clusters remain largely invariant within MIPS at fixed Pe ,

similarly to what we saw in Fig. 6 (d) and with the analysis of the number density of all kinds of defects. These results are in line with the absence of packing fraction dependence of other observables at fixed Pe within MIPS.

Solid and hexatic data are well represented by exponential decays $P(n) \propto e^{-n/n^*}$. For instance, at $Pe = 100$ we found that the scales in the exponential decay are $n^* \simeq 30$ in the solid and $n^* \simeq 50$ in the hexatic. The master curve for the MIPS data shows a much slower decay, suggesting a first power law cut-off at large sizes,

$$P(n) \simeq n^{-\tau_n} f(n/n^*), \quad (15)$$

with $f(x \gg 1) \rightarrow 0$. Although we lack a precise knowledge of the scaling function of the cluster size distribution, which renders the estimation of τ_n quite ambiguous, from the data in Fig. 17, we can infer $\tau_n \approx 2.2$ for the two Pe . The values of the average $\langle n \rangle \equiv \int_0^\infty dn n P(n)$ are also reported in Table III and decrease with increasing Pe . From the two panels in Fig. 17, where we used an exponential form for the function f , one sees that, consistently, the cut-off length n^* is a decreasing function of Pe .

Pe	$\langle \tilde{A}_H \rangle$	$\langle \tilde{A}_B \rangle$	$\langle n \rangle$	d_f
50	68.9	296.328	28.590	1.74 ± 0.04
100	151.7	378.894	26.360	1.66 ± 0.06
200	795.0	442.757	22.271	1.53 ± 0.08

TABLE III. Geometric parameters in MIPS. The averaged \tilde{A}_H and \tilde{A}_B were computed from the numerical data. Within our numerical accuracy $\tau_B \simeq 2.2$ [95] and $\tau_n \simeq 2.2$ at the three Pe and quite independently of ϕ (at least not too close to the lower spinodal). The average cluster size $\langle n \rangle$ is computed from the cluster size distribution $P(n)$ displayed in Fig. 17 and the fractal dimension is extracted from the analysis of the radius of gyration of the clusters, in Fig. 16.

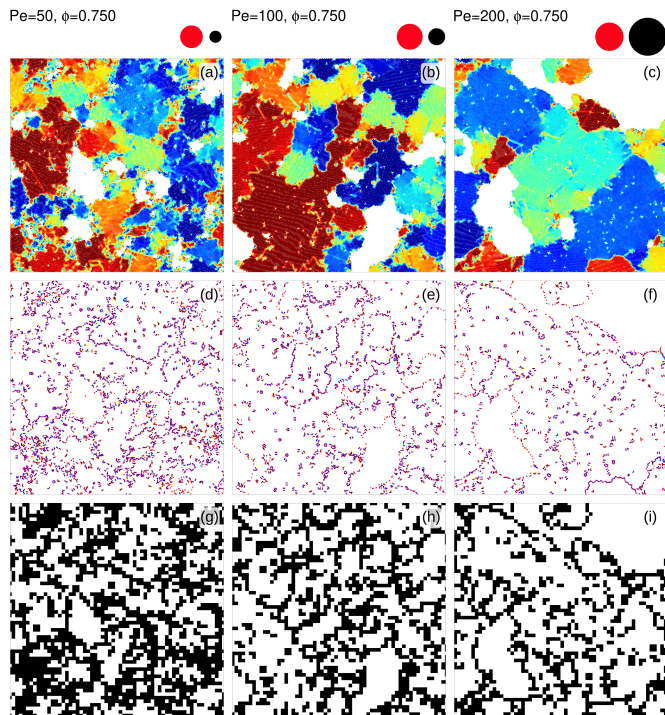


FIG. 18. Snapshots showing the influence of Pe on the topological defects (support to the data in Table III). In the three columns, $Pe = 50, 100, 200$ from left to right, all at $\phi = 0.75$. We eliminated the particles in the gas and we used a white background for the gas regions. First row: color map of the local hexatic order projected on the horizontal axis. Second row: only the defected particles are represented, showing the string-like structures located at the boundaries between domains with different orientation. Third row: clusters of defects after coarse-graining with $d_s = 3\sigma_d$. As Pe increases, the network structure gets sharper. The red and black disks on top of the plots represent the scales $\langle \tilde{A}_B \rangle$ and $\langle \tilde{A}_H \rangle$, respectively.

In Table III we report the average area of the hexatic domains, $\langle \tilde{A}_H \rangle$, gas bubbles, $\langle \tilde{A}_B \rangle$, and average cluster size, $\langle n \rangle$, together with the fractal dimension of the clusters of defects, d_f . A first observation is that while $\langle \tilde{A}_H \rangle$ grows, $\langle n \rangle$ decreases with Pe, which is compatible with the idea that the defect clusters are mostly located along

the boundaries between hexatic patches. A second remark is that d_f weakly decreases with Pe, suggesting that clusters get more string-like as Pe increases. This is in agreement with the inspection of snapshots, see, for instance, Fig. 18.

We stress here that the way in which we count the defects, excluding the boundaries between dense and gaseous regions, inhibits the possible percolation of defect clusters within MIPS. Indeed, if the network of grain boundaries within the MIPS drop percolated, we would observe different distributions at different densities concomitant with the growth of the dense drop size with ϕ . However, this does not happen, see Fig. 17. Instrumental to this result is the appearance of gas bubbles [95, 97] within the droplet which cut the defect network.

Finally,

- in the MIPS regime, we see hexatic domains, leaving behind a network of grain-boundaries, that can become large but remain finite. The topological defects are mainly located along these boundaries and the network is cut by the gas bubbles.

VI. MELTING AND PERCOLATION OF CLUSTERS OF DEFECTS

In Sec. IV we studied the densities of point-like defects, how they compare to the standard KTHNY theory of melting in passive systems, and their behavior in the presence of self-propulsion. Next, in Sec. V, we focused on MIPS and we characterized the aggregation of defects into a ramified non-percolating network. Now, we investigate in depth the collective behavior of defects.

For parameters close to the hexatic-liquid transition, most mis-coordinated cells cannot be identified as disclinations or dislocations, but appear in clusters comprising defects of alternating topological charge, see Fig. 2 and Fig. 20. These objects, when sufficiently large, lie beyond the KTHNY theory. Thus, quite naturally, we need to understand which role they play in the melting of the hexatic.

A related purpose of this Section is to investigate whether defect clusters show any qualitative difference depending on the first order (for very small Pe) or second order (for larger Pe) nature of the hexatic-liquid transition. For this reason, we also study Brownian particles with a soft interacting potential for which the melting transition in the passive limit has been shown to be continuous [23] (see also App. A).

A. Number densities

We start by comparing the number density of particles belonging to the different kinds of defects in the passive and active hard disk system, as well as in the soft particle passive one. Figure 19 shows that

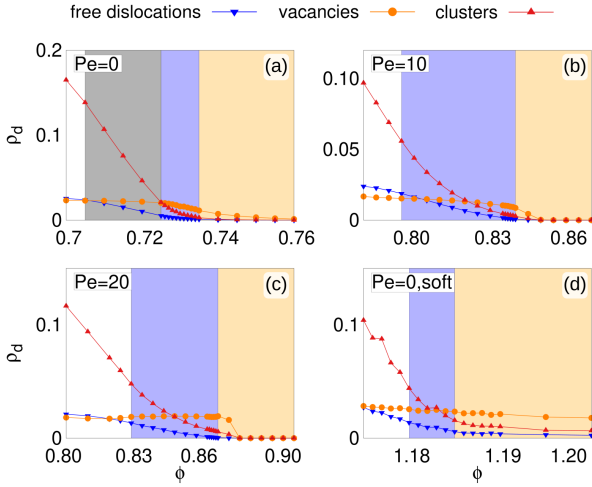


FIG. 19. Normalized number density of dislocations, vacancies and clusters, as a function of ϕ for passive hard disks (a), ABP at $Pe = 10$ (b) and $Pe = 20$ (c), and passive soft disks (d). The solid, hexatic, phase-coexistence and liquid regions are shown in orange, blue, gray and white, respectively.

- the number density of particles in clusters dominates the distribution of defects in the hexatic and liquid phases, proving that topological excitations are collective rather than localized in this sector of the phase diagram.

This also suggests that their proliferation might play an important role in the mechanism driving the melting of the hexatic, instead of (or at least in combination with) the unbinding of disclinations. Clusters of defects in hard-disk systems have been associated to the formation of grain boundaries delimiting regions of different hexatic order [23, 25], which could drive an alternative first-order melting mechanism in 2D [19–21]. For passive soft-disks and active hard disks at $Pe = 10, 20$, there is no evidence for a first-order transition, and yet the density of defected particles in clusters at the liquid-hexatic transition is very close to the passive hard-disk value (≈ 0.05). This suggests, as we show below, that the proliferation of clusters might be generic and not responsible for the first-order character of the hexatic-liquid transition of passive hard disks.

For soft particles, we found that the number density of isolated dislocations is different from zero at all ϕ (even in the solid), but its variation is faster below the transition, see Fig. 19 (d). Such behavior departs from a recent study reporting that the solid phase melting in a system of even softer Active Brownian particles is not driven by the proliferation of dislocations, as a KTHNY scenario would predict, opening the possibility of breaking orientational LRO in the absence of any defect [59]. For very hard disks (with thus very small mutual overlaps) the solid cannot melt in the absence of free dislocations, as our analysis clearly shows. However, particle softness influences strongly the nature of melting [23], as also shown

by the results in App. A. Under activity, the competition between the potential stiffness and self-propulsion is likely to affect even further the melting scenario. Although it is hard to make a quantitative comparison between the results in [59] and ours, because of the large difference in the potential considered, it is however surprising that these authors did not find a proliferation of defects in their solid phase.

B. The numerical percolation curve

In the study of defects in MIPS, we already treated the configurations with the coarse-graining procedure explained in Sec. III C. We apply here the same procedure to all defect clusters. Details on the effect of the coarse-graining linear length d_s are given in App. F.

Figure 20 displays, on the first row, configurations (after coarse-graining) within the hexatic-liquid coexistence region of equilibrium hard-disks, with the packing fraction decreasing from left to right. In the second row, we show configurations for $Pe = 20$ across the continuous hexatic-liquid phase transition. The largest coarse-grained defect clusters highlighted in yellow are finite, while the red ones percolate across the system size. In order to identify whether a cluster percolates in our periodic lattice (made of empty or occupied cells after coarse-graining), we applied the method designed by Machta et al. [75, 76]. We then use the framework of percolation theory [77], see Sec. VIB, to analyze the statistics of clusters of defects and argue whether critical percolation-like

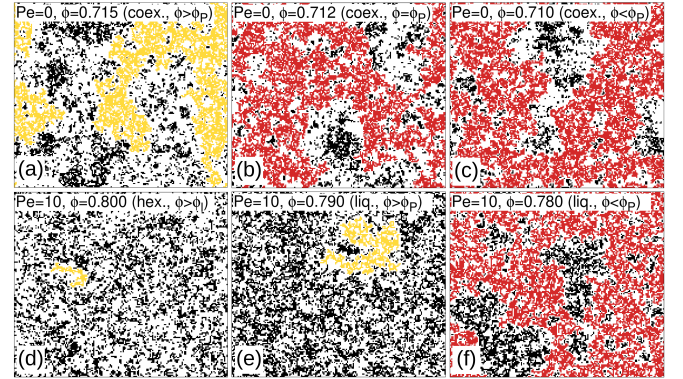


FIG. 20. Coarse-grained clusters of defects across the hexatic-liquid transition. Finite size clusters are painted in black. The largest cluster in the system is painted red or yellow, whether it percolates or not. The first row corresponds to equilibrium hard disks at packing fractions (a) $\phi = 0.715$ (in the coexistence region, above percolation), (b) $\phi = 0.712$ (in the coexistence region, at the onset of percolation ϕ_P) and (c) $\phi = 0.710$ (in the coexistence region, below percolation), spanning the coexistence region between hexatic and liquid. In the second row, we show ABP at $Pe = 10$, with (d) $\phi = 0.800$ (in the hexatic), (e) $\phi = 0.790$ (in the liquid, above percolation) and (f) $\phi = 0.780$ (in the liquid, below percolation). We recall that we use $d_s = 3\sigma_d$ as coarse-graining linear length.

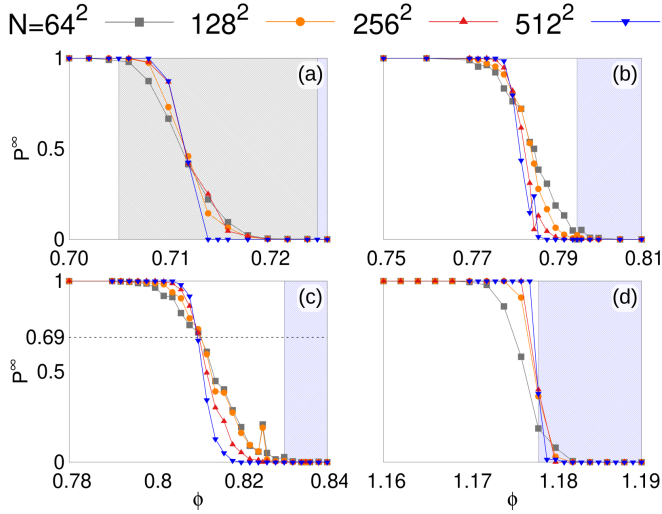


FIG. 21. Percolation probability P^∞ against the global packing fraction for different system sizes and fixed $Pe = 0$ (a), 10 (b), 20 (c) and $Pe = 0$ soft-disks (d). The curves cross at a point $\phi_P(Pe)$ that is identified as the percolation transition. The analytical prediction of the percolation probability at the critical point [99] is indicated by a horizontal dotted line.

behavior emerges in the system.

After the identification of percolating clusters in the snapshots, the aim now is to locate a percolation curve, $\phi_P(Pe)$, in the phase diagram (see the red symbols in Fig. 1). Figure 21 shows a finite size analysis of the percolation probability P^∞ as a function of the packing fraction for fixed Pe . All curves smoothly increase from 0 to 1 when ϕ decreases from high to low values, in the vicinity of the hexatic-liquid transition. As the system sizes increase the variation of P^∞ with ϕ becomes steeper and approaches a step function in the thermodynamic limit. The curves for different system sizes are thus expected to cross at a single point that we identify as the percolation critical point ϕ_P (see [78, 79] for a similar investigation of particle systems). The value of P^∞ at critical percolation on a square lattice with PBC has been computed in [99], yielding the value indicated by a horizontal dotted line in Fig. 21 (c). Such prediction matches noteworthy our numerical data for $Pe=10$, and remains consistent with the data in the other two cases, for which more data points around the onset of percolation would be needed to put the comparison into quantitative test.

The full analysis proves that

- clusters of defects percolate at a critical packing fraction $\phi_P(Pe)$. In equilibrium conditions, ϕ_P is located in the hexatic-liquid coexistence region for hard-disks and at the liquid-hexatic transition for soft-disks. In the active case, $\phi_P(Pe)$ lies below, but rather close to, the liquid-hexatic transition point. These conclusions are reached within our numerical accuracy,

More precisely, while for passive hard-disks ϕ_P is lo-

cated at $\phi \simeq 0.712$, in the middle of the coexistence region, for $Pe = 10, 20$ we find $\phi_P \simeq 0.780, 0.810$ respectively. The latter values are smaller than $\phi_l(Pe)$ (see the colored regions in Fig. 21 for a reference) and are thus located within the co-existence region ($Pe < 3$) or in the liquid phase ($Pe > 3$). For the passive soft-disks, percolation coincides with the hexatic-liquid critical point up to our numerical accuracy.

For larger Pe values, the system demixes by MIPS over a range of packing fractions, as shown in Fig. 1. For Pe values in between the MIPS critical point [94, 100] (located at around $Pe \approx 35$) and the intersection of the liquid-hexatic critical line with the MIPS coexistence region, percolation can also occur. As shown in Fig. 22 (a), the cluster size distributions $P(n)$ for $Pe = 50$ display distinctive features of percolation phenomena. Starting from the solid phase, where clusters have relatively small sizes and are exponentially distributed, the distribution broadens as ϕ is decreased and eventually becomes algebraic at $\phi = 0.815$, in between the hexatic-liquid transition, at $\phi_l = 0.855$, and the MIPS high density branch. The analysis of P^∞ is consistent with such behavior of $P(n)$. As shown in Fig. 22 (b), the probability of a percolating cluster increases fast as we enter the liquid phase from the hexatic, where P^∞ vanishes. However, P^∞ does not reach its saturating value $P^\infty = 1$ as it occurs in the absence of MIPS (see Fig 21). The growth of P^∞ is interrupted by MIPS. As anticipated in Sec. VB, MIPS prevents the percolation of clusters of defects via the formation of bubbles that are constantly reshaping. However, the system displays a power law decay $P(n) \sim n^{-\tau_n}$, with an exponent close to the one of 2D site percolation $\tau_n = 187/91 \sim 2.05 = \tau_n^*$ at a precise ϕ which we identify as the percolation point ϕ_P (We use this criterium here, rather than the finite-size analysis of P^∞ as we did for smaller Pe values.) See App. G for a detailed analysis of the structure of defect clusters at the percolation threshold for $Pe = 50$.

C. Radius of gyration and fractal dimension

We turn now to the characterization of the (possibly fractal) geometry of the clusters. Typical scatter plots of n_C against R_{g_C} are shown in Fig. 23 for the hard disk system. The data-points are taken at different Pe values and fixed packing fraction $\phi_P(Pe)$, the percolation curve determined in Sec. VIB. The relation between the mass and radius of gyration is in reasonably good agreement with the expectations from standard 2D critical percolation, for which $d_f = 91/48 \sim 1.90 = d_f^*$. The numerical estimates of the fractal dimension d_f extracted from such scatter plots for different Pe values at $\phi = \phi_P$ are reported in red, and at $\phi = 0.5$ in MIPS in black, in Fig. 24 (a). The data points are consistent with constant behavior on the curve $\phi_P(Pe)$ (red) while they have a weakly decreasing dependence on Pe in MIPS (black).

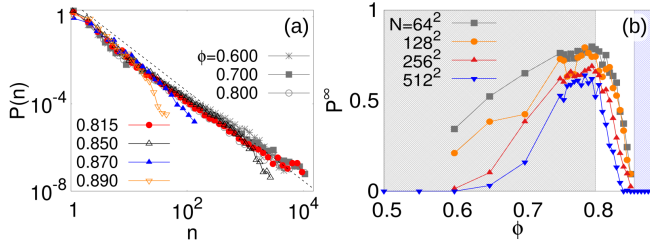


FIG. 22. (a) Size distribution of the defect clusters at fixed $Pe = 50$ and different values of the global packing fraction given in the key across the solid (orange symbols), hexatic (blue symbols) and liquid (black symbols) phases above the upper limit of MIPS. The dotted line corresponds to an algebraic decay with exponent $\tau_n = 187/91$. Red symbols correspond to the case $\phi = 0.815$ for which we observe a power-law distribution. (b) Percolation probability at $Pe = 50$ and different system sizes. Again, the blue region indicates the hexatic phase, the white one the liquid and the gray the coexistence region, here due to MIPS.

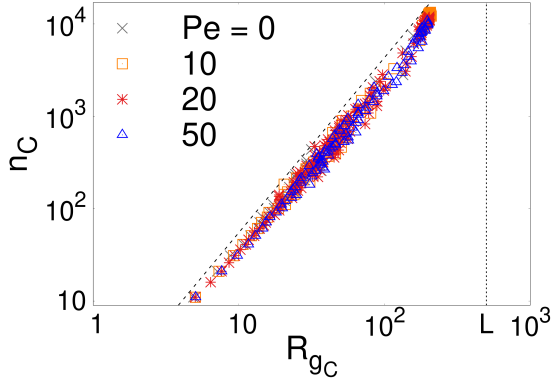


FIG. 23. Scatter plots of the size n_C against the radius of gyration of the clusters R_{gC} . The different data-points (colors) correspond to the different values of Pe given in the key. In all cases, the packing fraction is $\phi_P(Pe)$. The black dashed line corresponds to $n_C \approx R_{gC}^{d_f}$, with $d_f = 91/48$. The vertical dotted line corresponds to the linear size $L \approx 500$ of the system.

D. Cluster size distribution

The full analysis of clusters, in view of percolation theory, leads us to carefully reconsider their size distributions $P(n)$. These are obtained by measuring the number of coarse-grained clusters made of n defected cells, excluding the spanning one.

In Fig. 25 we show $P(n)$ for passive hard disks (a), ABP at $Pe = 10$ (b), $Pe = 20$ (c), and passive soft disks (d). In all cases, we show results for different ϕ across all phase transitions. Starting from the solid (orange symbols), the effect of decreasing ϕ is clear, as the distribution broadens to include larger clusters. The data in the hexatic phase (in blue) also follows this trend. The key feature to highlight here is that, in all cases – for passive

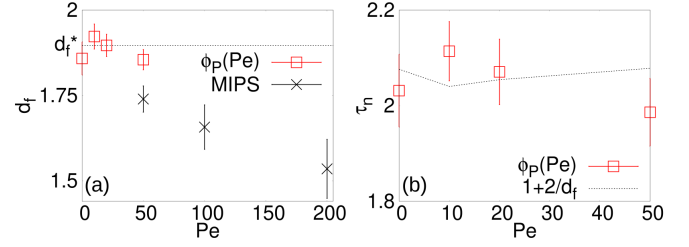


FIG. 24. (a) The fractal dimension d_f of the defect clusters as a function of Pe for global densities along the $\phi_P(Pe)$ curve away from MIPS (in red), and within MIPS at $\phi = 0.5$ (in black). The dotted line is at $d_f^* = 91/48 \approx 1.90$, the value of uncorrelated site percolation on a 2D lattice [77]. (b) The exponent τ_n was evaluated from the algebraic decay of the cluster size distribution at the percolation critical point, ϕ_P , away from MIPS. The black dotted line is the value of τ_n extracted from the scaling relation in Eq. (10), using the values of d_f reported in (a).

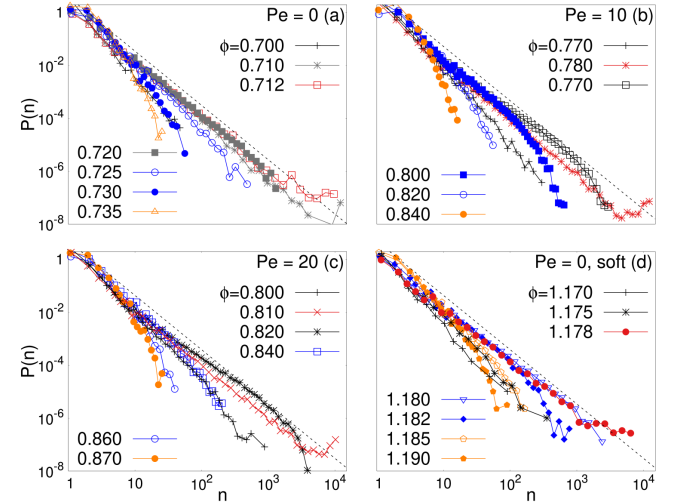


FIG. 25. Cluster size distribution for (a) passive hard disks, (b) passive soft-disks, (c) ABP at $Pe = 10$ and (d) ABP at $Pe = 20$. The different sets of data correspond to different ϕ given in the keys. The curve that we identify with critical percolation behavior is represented in red. An algebraic decay $P(n) \propto n^{-\tau_n}$ with $\tau_n = 187/91$ is plotted with dotted black lines in all panels. At criticality, the Fisher exponent τ_n is related to space dimension and the cluster fractal dimension via Eq. (10), see Fig. 24. All the panels represent the data on the same scale on both the vertical and horizontal axis.

disks, both hard and soft, and also active ones – $P(n)$ becomes *scale free* at a packing fraction slightly below ϕ_l , the value below which orientational correlations decay exponentially (red data). This is the hallmark of percolation. Consistently, the packing fraction at which the distributions become scale-free coincides with the value ϕ_P extracted from the finite-size analysis of P^∞ . As already mentioned, percolation is observed: (i) in the middle of

the coexistence region for equilibrium hard disks (corresponding to the intersection point of the Binder cumulant associated to hexatic order obtained for different system sizes [24]), (ii) at the hexatic-liquid transition for equilibrium soft disks, (iii) slightly below the hexatic-liquid transition for ABP.

At a critical percolation point, the scaling relation $\tau_n = 1 + d/d_f$, must hold. As our analysis demonstrates, our coarse-grained clusters of defects at ϕ_P follow this scaling. The algebraic decay $n^{-\tau_n}$, with $\tau_n = 187/91$ – the exponent corresponding to random site percolation in 2D, for which $d_f = 91/48$ – captures the behavior of $P(n)$ at ϕ_P , see Fig. 25. Thus,

- at $\phi_P(\text{Pe})$, the statistics of the coarse-grained clusters is well described by critical percolation, irrespective of the discontinuous (for passive hard disks [22]) or continuous (for passive soft disks [23] and ABP at $\text{Pe} = 10, 20$ [24]) character of the hexatic-liquid transition.

At $\phi_P(\text{Pe})$ the measurement of d_f provides a consistent prediction for the Fisher exponent τ_n characterizing the distribution of cluster sizes $P(n)$. This is confirmed by the data presented in Fig. 24 (b)-(c). The Fisher exponent extracted from the decay of $P(n)$ at ϕ_P is reasonably close (considering the difficulty of such numerical measurements) to the value predicted by the scaling relation (10), using the value of d_f obtained independently from the mass-radius of gyration relation. In the MIPS

sector, though, such scaling is likely to be lost. First, clusters do not percolate inside MIPS. Secondly, as already discussed, the numerical determination of τ_n from the size distributions is somehow ambiguous. The algebraic decay of $P(n)$ expands on rather short scales only and the exponent seems to be independent of Pe while d_f appears to decay with Pe .

The percolation of coarse-grained clusters is illustrated in Fig. 20. For hard-disks in their equilibrium hexatic phase, the largest cluster (yellow) does not span the system. As we decrease ϕ , the size distribution broadens until a percolating cluster arises (red), right in the middle of the liquid-hexatic coexistence region [24]. The spatial location of the percolating structure is correlated with the one of the liquid as we explain in the next Subsection.

E. The emergence of the liquid

The correlation between the location of the defect clusters and the emergence of the liquid is proven by its comparison to the maps of the local density

$$\phi_i = \phi(\mathbf{r}_i) = \frac{\pi\sigma^2}{4A_i}, \quad (16)$$

with A_i the area of the Voronoi cell attached to the i th particle, and the maps of the local hexatic order parameter defined in Eq. (4).

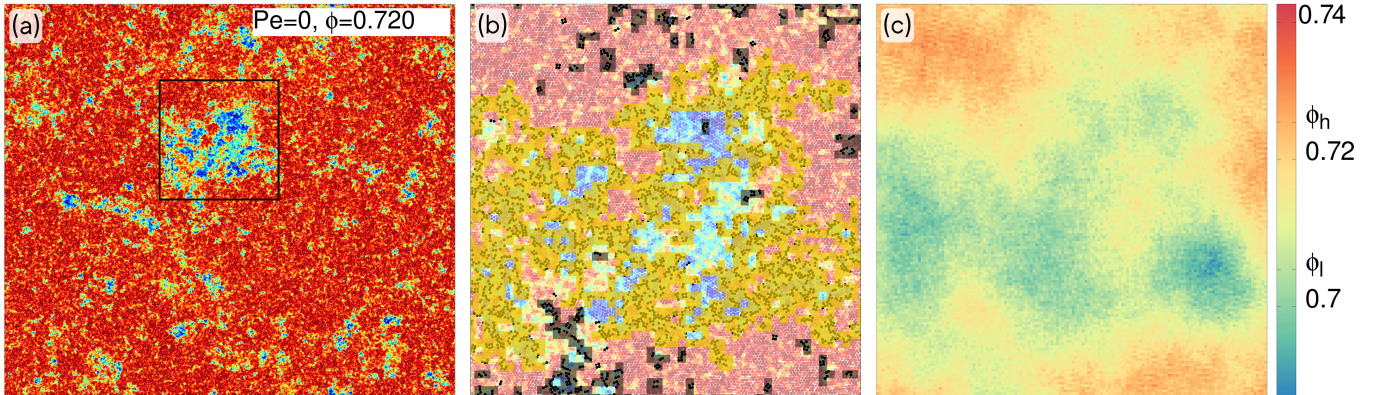


FIG. 26. (a) Color map of local hexatic order parameter (see the main text and [24] for the color code), for a hard disk system with $\text{Pe} = 0$ and $\phi = 0.720$, within the hexatic-liquid coexistence region and close to the high-density binodal. The red area is oriented along the mean orientation of the sample and corresponds to its hexatic region, in coexistence with the liquid one. (b) Detailed view of the zone surrounded by the black square in (a), showing a drop of liquid coexisting with the hexatic phase that largely surrounds it. Black cells are finite-size defect clusters. Yellow cells belong to the biggest (although finite) cluster of defects (see also Fig. 20). (c) Local density ϕ_i corresponding to (b) then coarse-grained over a length of $20\sigma_d$. The liquid and hexatic coexistence densities, appearing in the scale on the right are $\phi_l = 0.705$ and $\phi_h = 0.725$. A clear correlation between the location of the biggest cluster in yellow in panel (b) and the appearance of the liquid in panel (c).

In Fig. 26 we exhibit how the growth of the liquid

within the hexatic occurs in correspondence with the pro-

liferation of clusters of defects, in a passive system with a global packing fraction within the coexistence regime. Panel (a) displays the map of the local hexatic order parameter. In this plot we use the following convention: red particles are oriented along the horizontal direction, blue the opposite one, and the intermediate directions follow the code in panel (a) of Fig. 27. The square box selects a region of the system that is zoomed over in (b). In this sub-region a liquid drop co-exists with the hexatically ordered surrounding. The black cells are small size coarse-grained defect clusters while the yellow ones belong to the largest defect cluster in this region. The correlation between the location of the largest defect cluster and the liquid zone is confirmed in (c). In this latter case, the map of the local density is plotted according to the color code on the right bar, also indicating the values of the liquid and hexatic coexisting packing fractions.

We conclude that

- For parameters in the co-existence region of the equilibrium hard-disks system, the emergence of a percolating defect cluster can be attributed to the percolation of the liquid domain.

In Fig. 27 we present further evidence for such correlation in an active system at $Pe = 20$, close to the hexatic-liquid transition. Panel (a) presents the color map of the local hexatic order parameter, with red indicating the averaged, and also the majority, orientation in the system. As evidenced in the selected view Fig. 27 (b), which zooms over the box in (a), most defects are located at boundaries between different hexatic orders, where the hexatic melts *cfr.* Fig. 20 (b) and Fig. 27 (a). In short, Fig. 27 (a)-(b) suggests that

- at the continuous hexatic-liquid transition at intermediate Pe , coarse-grained clusters can be identified with grain-boundaries between regions with different orientational order.

Percolation in this case is associated with the emergence of a system-spanning cluster of defects, along which the liquid phase develops. For $Pe = 20$, there is no liquid-hexatic coexistence, and yet there is percolation slightly below the hexatic-liquid transition. For equilibrium soft-disks, the liquid-hexatic transition is continuous and accompanied by the percolation of clusters of defects.

F. Is critical percolation of defects driving melting?

Experience teaches us that one has to be extremely careful before claiming that there is a strict relation between a thermodynamic phase transition driven by the competition between interactions and fluctuations, such as melting, and a phenomenon of purely geometric nature, like percolation. In many lattice spin models, the properties of their second order thermal phase transitions can be rigorously described in terms of the critical percolation of suitably defined Fortuin-Kasteleyn (FK) clusters, that *are not* the obvious geometric ones one could

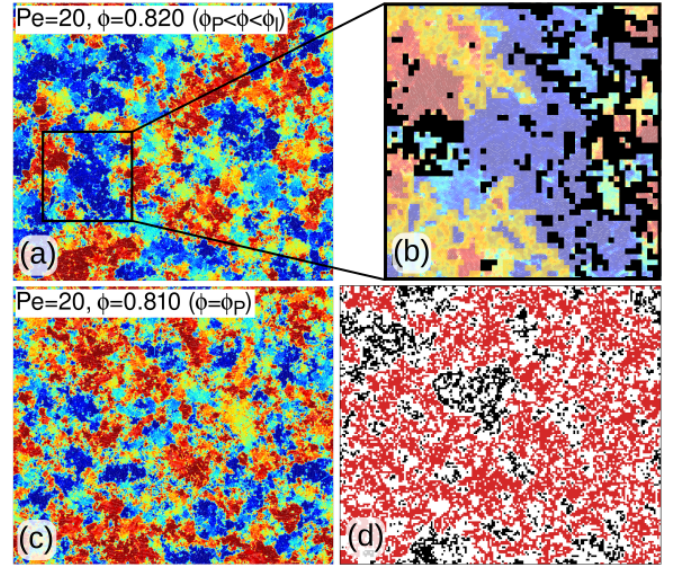


FIG. 27. (a) Map of the local hexatic order parameter $\psi_6(\mathbf{r})$ projected on the mean orientation of the system for active, $Pe = 20$, hard disks close to the hexatic-liquid transition ($\phi_l = 0.830$), within the liquid phase. (b) Zoom over the region within the black square in (a) with the defect cluster shown in black on top of the $\psi_6(\mathbf{r})$ background. (c) Map of the $\psi_6(\mathbf{r})$ projection at $\phi_P(Pe = 20) = 0.810$. (d) Clusters of defects in the configuration in (c) with finite ones in black and the percolating one in red.

a priori try to use [77, 101]. Moreover, although the FK clusters should not be useful to describe a first order thermodynamic transition, in cases with very long correlation lengths such as the 2D Potts model with $Q \gtrsim 4$, one could easily see them percolate close to the transition in finite size samples [102].

Our simulations of finite, off-lattice, particle systems, provide clear evidence that active, passive, continuous and discontinuous hexatic-liquid transitions are accompanied by the percolation of coarse-grained defect clusters. However, we should stress that the particle problem we are dealing with is defined in the continuum and, in addition to the *provisos* exposed in the previous paragraph, we face the difficulty of having to transform the particle configurations into lattice ones via coarse-graining.

We cannot therefore posit that the relevant clusters to describe the transition quantitatively are the coarse-grained defect ones we used. Still, albeit we cannot establish a rigorous link between melting and the geometric transition, the identification of a critical percolation phenomenon sheds new light on the microscopic mechanisms driving 2D melting, as the liquid phase does indeed emerge from the defect clusters similarly to the pre-melting of 3D colloidal crystals [30].

VII. CONCLUSIONS

We close the paper with a concluding Section that we divide in two parts. In the first one we recall the context in which our work inscribes, that is, the melting of spherically symmetric particle systems. In the second one we present a short summary and discussion of our results.

A. Context

In order to consider our results in the right perspective, we first observe that passive melting is a fundamental natural process and that local but also extended defects play a key role in it.

While the main mechanism for bulk 3D melting, as one in which the liquid pervades the system along grain boundaries between crystalline domains, is fully accepted, the one(s) leading to 2D melting are far from being fully understood.

Three dimensional experiments demonstrate the pre-melting along grain boundaries in the bulk of crystalline passive materials [30]. They thus prove that this is the basic mechanism promoting the direct melting transition from the crystal to the liquid. Besides, thermodynamic measurements reveal that the 3D melting transition is a conventional first order one [8].

One of the predictions of the KTHNY theory for 2D melting [11–13], the fact that the transition takes place in two steps with an intermediate hexatic phase is by now widely accepted. Experiments in a host of different materials have established the existence of this intermediate phase with QLRO. Early [82, 103] and more recent [14, 104, 105] experiments providing the necessary evidence are discussed in the review articles [5–10]. It is important to stress, though, that some other materials with different interactions, conform better [10] to Chui’s single first order transition arising through grain boundary melting even in 2D [20].

The KTHNY theory [11–13] also predicts the order of, and mechanisms for, the two transitions; basically, BKT singularities [81, 106] due to the unbinding of rather simple defects: dislocations in the solid-hexatic and disclinations in the hexatic-solid. Admittedly, experimental and numerical proofs of these predictions have remained elusive. In the terms of von Grünberg, Keim and Maret “...the colloid KTHNY literature on this point is full of irritating and partly contradictory findings” [7].

Experimental studies of the defect mediated scenario for the two step transition appeared in [104] where a substrate-free dipolar system was monitored and in [85], also reported in [10], where a monolayer of a repulsive colloidal system was studied. Based on a qualitative analysis of data, Kusner et al. [104] claimed that free dislocations appear in the hexatic, and free disclinations at the liquid-hexatic transition, with no signature of defect cluster formation. In [85], the free dislocation and free disclination densities detach from zero at different val-

ues of the packing fraction. While the latter is in rather good agreement with the critical value estimated from correlation and susceptibility measurements, the former is displaced towards a higher packing fraction compared to the one deduced from the translational susceptibility peak. The density of free dislocations is compatible with the KTHNY criticality with $\nu = 0.37$ while there is no quantitative analysis of the density of free disclinations. Other experimental papers, like the ones by Tang et al. [82, 83], report the appearance of dislocation loops and complex clusters in the free expansion melting of 2D charged colloidal micro-spheres and cast some doubt on the hexatic-liquid transition being solely driven by the dissociation of dislocations.

Being the collection of clean experimental data so hard, progress in this field came from numerical simulations which indicate that, for sufficiently hard disks, the transition from the hexatic to the liquid is of first order instead of BKT [22]. The measurements in this reference, and most following articles studying this hexatic-liquid transition, see, e.g. [23, 24, 27, 107–110], focused on macroscopic observables which do not provide clues about the mechanisms driving the phase transition.

Arguments for extended, possibly percolating, defect clusters which could render the transitions first order have been put forward by various authors. This proposal is an old debated topic, see e.g. [7, 103, 111], which has received renewed interest [23, 27, 31, 32, 112] after the Bernard & Krauth work [22], which differentiates the order of the hexatic-liquid transition from the one of the solid-hexatic. Although there is some numerical evidence for the proliferation of defects and their clusterization close to the hexatic-liquid transition of both passive [27, 32, 113] and active [59] 2D systems, we have found no quantitative support for, nor evidence against, the percolation of defect clusters at, or close to, this transition.

The geometrical description of phase transitions, such as the one provided by percolation of the rightly identified objects (be them fully geometrical or also partially statistical) is very appealing. Its search drives research efforts in different fields of material science (jamming, gelation, complex systems, etc.). It is therefore quite clear the interest in trying to elucidate whether a geometric phenomenon is behind the breakdown of the hexatic phase in 2D particle systems.

B. Summary of results

We provided the first quantitative numerical analysis of topological defects in 2D passive and active Brownian particle systems, reaching conclusions that confirm the classical KTHNY scenario concerning the solid-hexatic transition, but lie beyond it regarding the hexatic-liquid one.

Concretely, we characterized the melting of passive and active disks in terms of the statistics and spatial organi-

zation of point-like topological defects and the statistics and geometry of the clusters they form.

On the one hand, we found that the KTHNY scenario of dislocation unbinding gives a qualitative and quantitative description of the solid-hexatic transition of the hard disk system for all activities. Our measurements point towards the universality of this phase transition in the sense that the BKT scaling holds and the exponent ν is, within our numerical accuracy, equal to 0.37 all along the solid-hexatic transition line. It would be worth proving this statement analytically, possibly extending the analysis in [114] to a model with energy injection. This project goes beyond the scope of this publication.

On the other hand, we generically observed percolation of clusters of defects at the vicinity of the hexatic-liquid transition: within the coexistence region for equilibrium hard disks, at the transition for soft ones, and below the transition for active hard disks. The particles involved in the clusters overwhelm in number those participating in the dissociation of dislocations, which also exist as soon as the liquid phase appears. The fewer disclinations we identify are always very close to extended defect clusters and are not free to move in the sample. The geometry of the percolating cluster appears to be quite independent of the activity and very close to the one of conventional uncorrelated percolation in 2D.

Although defect cluster percolation has been associated to first-order melting scenarios in the past, we found it across both first and second-order transitions, in- and out-of-equilibrium. In all these cases, we found that the clusters of defects appear and grow in regions of density depletion and where interfaces between patches with different orientational order sit. The liquid starts permeating the sample from these spots.

What is the relationship between melting, a phase transition driven by the competition between interactions and fluctuations, and percolation, a phenomenon of pure geometric nature? In the context of classical spin systems, the connexion between thermal phase transitions and the percolation of suitably defined clusters can be rigorously established through, for instance, the Fortuin-Kasteleyn (FK) representation, which exactly maps a spin system on a geometric model [101, 115, 116]. We do not have a way to faithfully represent a system of interacting particles in terms of geometric clusters and, therefore, we cannot establish a rigorous connexion between melting and percolation. However, all the results reported point in the direction of suggesting the existence of such a relation.

At high Pe , MIPS prevails over the hexatic-liquid transition, and clusters of defects are large and ramified but, in the way we defined and counted them, do not percolate. Indeed, the dense MIPS droplet is also filled with gas bubbles with an algebraic distribution of sizes that disconnect the defect clusters at all packing fractions, even beyond the hexatic-liquid transition inside MIPS. Then, our defect cluster size probability distribution depends on Pe but not on the global packing fraction.

In short, we presented an unprecedented comprehensive analysis of topological defects in the stationary regime of 2D passive and active Brownian particles. We clarified the nature of the phase transitions in a way that sheds new light on the old problem of 2D melting, going beyond the KTHNY picture, and showing that percolation is an underlying phenomenon associated to 2D melting, both in equilibrium and non-equilibrium conditions. With a robust scaling analysis we characterized the statistic and geometric properties of the defect clusters and we found universal features along the critical percolation curve $\phi_P(Pe)$. We also proved the important role played by the dynamic bubbles in cavitation in the dense MIPS phase. They break the network of defects which lie mostly on the interfaces between micro-domains with orientational order.

ACKNOWLEDGMENTS.

We thank L. Berthier, C.B. Caporusso, C. Miguel, M. Picco, A. Suma, J. Tailleur and F. van Wijland for very useful discussions. We acknowledge access to the MareNostrum Supercomputer at the BSC, IBM Nextscale GALILEO at CINECA (Project INF16-fieldturb) under CINECA-INFN agreement and Bari ReCaS e-Infrastructure funded by MIUR *via* PON Research and Competitiveness 2007-2013 Call 254 Action I. DL acknowledges Ministerio de Ciencia, Innovación y Universidades MCIU/AEI/FEDER for financial support under grant agreement RTI2018-099032-J-I00. LFC acknowledges financial support from ANR-THEMA (AAP CE30). IP acknowledges support from Ministerio de Ciencia, Innovación y Universidades MCIU/AEI/FEDER for financial support under grant agreement PGC2018-098373-B-I00 AEI/FEDER-EU and from Generalitat de Catalunya under project 2017SGR-884, and Swiss National Science Foundation Project No. 200021-175719.

Appendix A: Soft disks

In this Appendix we present some details on the behaviour of the passive soft disk system.

In Fig. 28 (a) we show the orientational correlation function (built with the hexatic order parameter measured at two points in space separated by a distance r). The different colors follow the code used in the main text, that is, blue for hexatic and black for liquid. In the main part of panel (b) we present the equation of state, $P(\phi)$, for soft disks and we compare it to the one of hard disks, displayed in the inset. The absence of a loop in the curve in the main panel, replaced by an inflexion point, indicates that the hexatic-liquid transition is continuous for soft disks. The comparison with the hard-disk $P(\phi)$ in the inset, obtained as a detailed view of Fig. 2 (a) in [24], makes this fact clear.

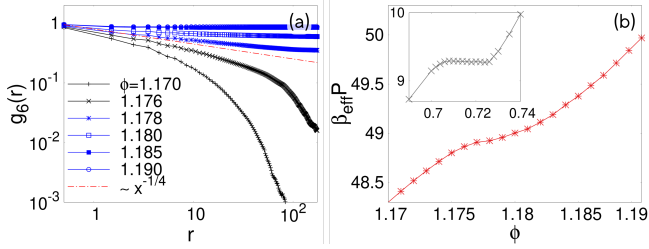


FIG. 28. Soft disks in equilibrium. (a) Orientational correlation function. Consistently with the colour code used in the main text, black curves are for parameters in the liquid phase, while blue curves are used for the hexatic. The red straight line is the critical power-law predicted by HNY for the liquid-hexatic BKT transition [11]. (b) Monotonically increasing equation of state in the region across the liquid-hexatic transition. In the inset, the equation of state for hard disks at equilibrium, obtained in Ref. [24], with the loop pointing towards the direction of a first order phase transition in this case.

Appendix B: Particle clustering

The identification of a particle cluster in a continuous system is not unique and several proposals for ways to do it have been summarized in [117]. We adopted a definition based on the proximity between the particles concerned in configurational space (similar to the Stillinger clusters of liquids). More precisely, we identified particle clusters using the Density-Based Spatial Clustering of Applications with Noise (DBSCAN) [118]. With the chosen parameters for the DBSCAN algorithm, one particle is considered to belong to a cluster whenever it has at least 12 neighbors within a radius of $2.1 \sigma_d$ with σ_d the particle diameter (that is slightly above the third shell radius of the triangular lattice). In this way we pinpointed the dense phase in MIPS.

Appendix C: Finite size effects

In Fig. 29 we show that the counting of particles belonging to dislocations and disclinations is not much influenced by finite size effects. Indeed, the number density of dislocations and disclinations do not vary much with the sizes of the systems. The measurements were done on independent systems with the sizes given in the keys. Although *a priori* quite surprising, a similar lack of strong finite size effects was observed in the counting of vortices in the disordered phase of the 2DXY model [119].

We see a similar size independent in the pair correlation functions (not shown here).

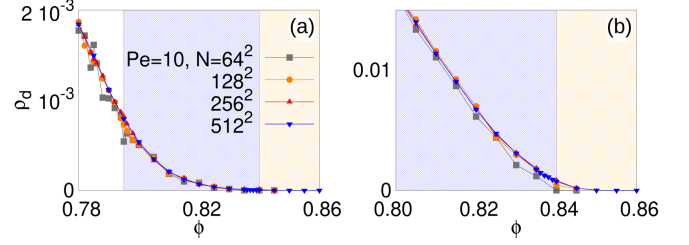


FIG. 29. Finite size effects on the number densities of point-like defects, as defined in Eq. (5). (a) Dislocations. (b) Disclinations. The system sizes are given in the key.

Appendix D: Improved fits of point-like defect densities

We have shown in Sec. IV that the behavior of free dislocations close to the solid-hexatic transition is altogether compatible with the KTHNY unbinding mechanism, so that the number density of free dislocations is strongly related to the spatial divergence of the hexatic correlation length predicted by the theory.

Here we provide an additional analysis of the critical behavior of the number density of dislocations, in order to determine a reliable uncertainty interval for the non-universal values of the parameters given in Tables I and II.

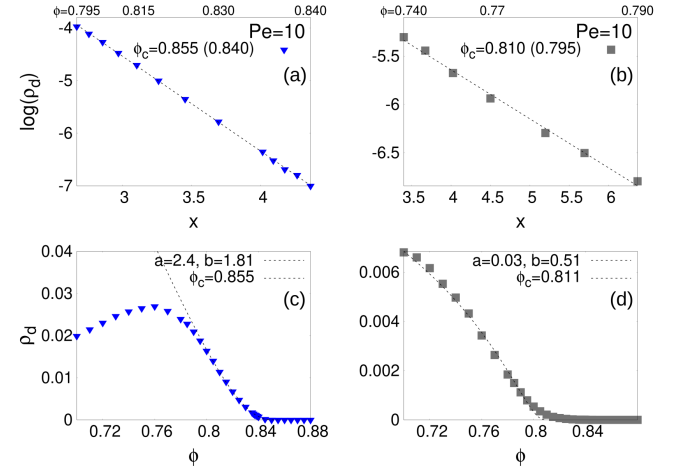


FIG. 30. In the first row, the linear representation, Eq. (D1), of the point-like defects at $Pe = 10$ with $x = [\phi_c/(\phi_c - \phi)]^\nu$. (a) Dislocations with $\nu = 0.37$ and (b) disclinations with $\nu = 0.5$. ϕ_c is chosen to take the values shown as labels in the panels. Between parenthesis the values of ϕ_h and ϕ_l estimated from the study of correlation functions and local densities. In the second row, the result of the linear fit fixing the remaining parameters a and b .

Let us first analyze the free dislocation number densities. Starting from the full BKT critical form in Eq. (11), we fix the value of the critical exponent $\nu = 0.37$ predicted by HNY for the solid-hexatic transition, and we

consider the new variable $x = [\phi_c/(\phi_c - \phi)]^\nu$, so that the logarithm of the number density of dislocation obeys the linear relation:

$$\log \rho_d = \log a - bx. \quad (D1)$$

As shown in the first row in Fig. 30 for $Pe = 10$, we find that, interestingly, the numerical data for dislocations do indeed follow a linear behavior if we tune the value of ϕ_c around the initial guess ϕ_h , given from the analysis of the translational correlation functions in [24], and recalled in Table I. Moreover, the optimal value of ϕ_c which reproduces the linear prediction is really close to the one computed with the fit of the data to the full expression in Eq. (11), also given in Table I. On the one hand, this proves the robustness of the fitting procedure presented in the text. On the other hand, it serves as an alternative procedure to obtain an independent estimation of the parameters a and b and their related errors. Moreover, the results of this (linear) evaluation, given in the key of Fig. 30, are not affected by the complexity of a full non linear fit of the stretched exponential form of Eq. (11).

We also show in the second row in Fig. 30 the same analysis for the number density of disclinations across the liquid-hexatic transition, being now the fixed value of the critical exponent the one of the standard BKT transition $\nu = 0.5$. Similar results as the ones discussed above for dislocations apply to the disclinations as well. The parameters of the full fit are given in Table II.

Appendix E: Four parameter fits

In Tables IV and V we display the values extracted from four-parameter fits to the dislocation and disclination number densities close to the solid-hexatic and hexatic-liquid transitions, respectively. In these fits we

Pe	ν	a	b	ϕ_c	ϕ_h	χ^2/ndf
0	9	13	0.002	1	0.735	0.920
10	0.6	0.4	0.7	0.857	0.840	2.89
20	0.3	5	3	0.881	0.870	1.39
30	0.8	0.2	0.3	0.909	0.880	2.08
40	0.7	0.2	0.4	0.90	0.885	0.924
50	0.2	7	3	0.892	0.890	0.461

TABLE IV. Dislocation unbinding at the solid-hexatic transition. The fitting parameters in Eq. (11) for the density of free dislocations plotted in Fig. 7. In the table above, ν is also a fitting parameter. The values of $\phi_h(Pe)$ are the ones estimated from the analysis of the correlation functions and probability densities in [24].

used the BKT scaling form in Eq. (11) and we also let the exponents ν be determined by the fits. The fitting intervals and number of data points considered are the same as the ones used in the main text and in App. D. The curves resulting from these four parameter fits are

Pe	ν	a	b	ϕ_c	ϕ_l	χ^2/ndf
0	0.4	0.4	2	0.7	0.725	3.24
10	2	0.012	0.03	0.85	0.795	0.859
20	1	0.02	0.2	0.9	0.830	0.858
30	0.3	0.09	2	0.86	0.845	0.965
40	2	0.013	0.01	0.96	0.850	0.661
50	0.9	0.008	0.1	0.88	0.855	0.288

TABLE V. Disclination unbinding at the hexatic-liquid transition. The fitting parameters in Eq. (11) for the density of free disclinations plotted in Fig. 8. In the table above, ν is a fitting parameter. The values of $\phi_l(Pe)$ are the ones estimated from the analysis of the correlation functions and probability densities in [24].

drawn as broken lines in Fig. 7 and Fig. 8 for dislocations and disclinations. The results in the Tables are not satisfactory for several reasons. First of all, some values of ν are unrealistic (e.g., $\nu = 9$ at $Pe = 0$ for dislocations and $\nu = 2$ at $Pe = 40$ for disclinations). More generally, they do not show any regular trend. The same lack of regular trend can be observed in the fitted values of the critical packing fractions ϕ_c , which show an oscillating behaviour as a function of Pe in both cases. Moreover, in some cases they are unrealistically large and close to ϕ_{cp} . The χ^2 normalized by the number of degrees of freedom, is an indicator of the quality of a fit. However, a fit with four rather than three parameters will lead to a better χ^2/ndf without necessarily implying that it is a better fit. Indeed, if one looked in more detail into the errors incurred with this kind of fit, one would find that they are too large and hence not acceptable. The failure of the fits with too many free parameters gives further support to the procedures followed in the main text and in App. D, in which we fixed ν and we searched for ϕ_c .

As an additional test of reliability of our fits, we also tried a similar fitting procedure in which we fixed ν to different values, around the expected HNY critical value. Increasing ν beyond 0.37 and 0.5 for dislocations and disclinations we observed a drift of the fitted ϕ_c away from the ϕ_h and ϕ_l , respectively. Instead, decreasing ν below these values leads to unstable and unrealistic values for the other fitting parameters.

Appendix F: Effects of coarse-graining

In Sec. III we introduced a coarse-graining procedure, with coarse-graining length d_s , to fill the microscopic gaps between defects and identify the coarse-grained clusters.

We first study the effect of such a coarse-graining on the number of unpaired defects. The critical behaviour of the number density of dislocations in a system at $Pe = 10$ for different coarse-graining lengths $d_s = 0, 2, 3, 5$ (in units of σ_d), is zoomed over in Figs. 31. For dislocations, we see that the three parameter fits to Eq. (11) with $\nu = 0.37$ are very satisfactory for all these values

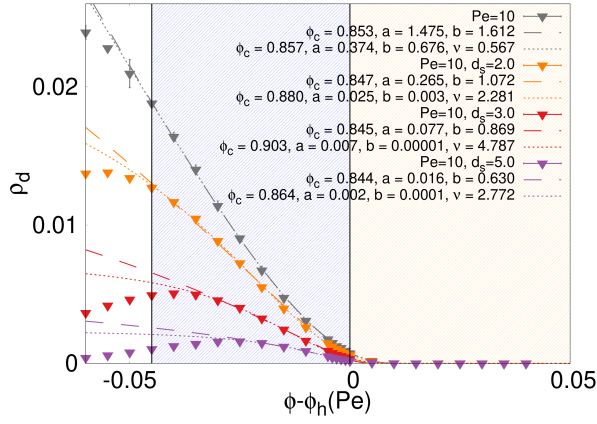


FIG. 31. Effect of coarse-graining on the critical behavior of the number density of dislocations at $Pe = 10$. Raw data and four (dotted) and three (dashed) parameter fits to the form in Eq. (11). The coarse-graining length increases from top to bottom, $d_s = 0, 2, 3, 5$. The vertical line on the left is the limit of the fitting interval in the case with no coarse-graining. In the other cases the fit is done on the data-points to the right of the maximum. The values of the four and three parameter fits are given in the key.

of d_s . Moreover, the ϕ_c 's extracted from the fits slowly approach the value $\phi_h = 0.840$ estimated in [24] for $Pe = 10$. Instead, the four parameter fits in which ν is also an adjustable parameter yield unreasonable values of ν and, moreover, no clear trend for ϕ_c . The fitting parameters are given in the key.

Instead, for the number density of disclinations displayed in Fig. 32 the effect of the coarse-graining length is stronger. Already for $d_s = 3$ we have practically erased all disclinations. The three parameter fits with $\nu = 0.5$ to the two remaining sets of data, with no coarse-graining and using $d_s = 2$, are of better quality than the four parameter ones.

Finally, in Fig. 33 we display the effects of coarse-graining on the isolated defect counting in the soft disk system at $Pe = 0$. Blue and gray data-points are for dislocations and disclinations, respectively, and the dotted curves represent the raw data with no coarse-graining. The figure proves that the excess presence of dislocations in the solid phase is strongly diminished as soon as we apply a coarse-graining over a rather short scale, $d_s = 2$.

In Fig. 34 we study the coarse-graining length influence on the percolation properties. In panel (a) we see that the finite size scaling of the percolation probability P^∞ depends on d_s and the crossing point, ϕ_P , moves towards ϕ_l for increasing d_s . Still, the critical properties of the defect clusters are independent of d_s in the sense shown in panel (b): the cluster size probability $P(n)$ keeps the same algebraic decay when measured at the corresponding ϕ_P .

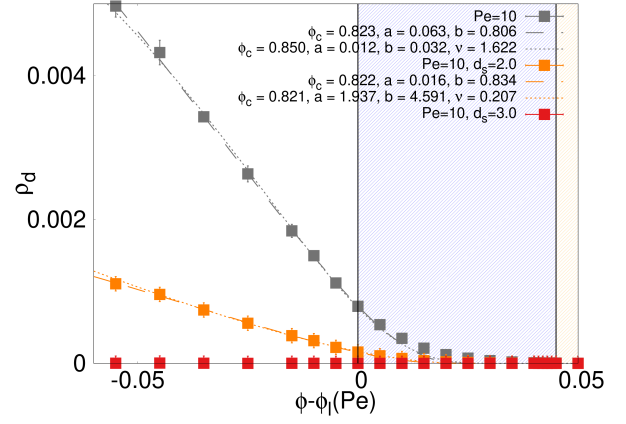


FIG. 32. Effect of coarse-graining on the critical behavior of the number density of disclinations at $Pe = 10$. Raw data and four (dotted curves) and three (broken curves) parameter fits to the form in Eq. (11). The values of the four and three parameter fits are given in the key.

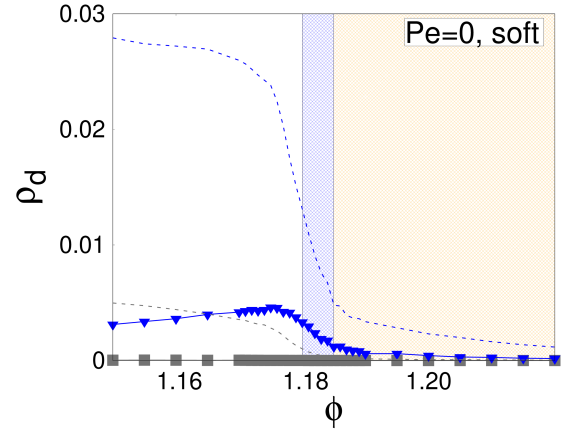


FIG. 33. Effect of coarse-graining with $d_s = 2$ on the point-like defect counting in a passive system of soft disks. The dotted curves show data with no coarse-graining applied.

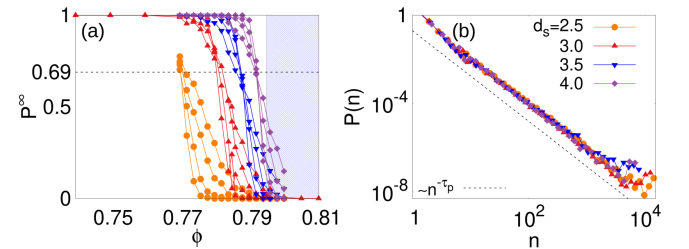


FIG. 34. Active hard disk system at $Pe = 10$. (a) The cluster size probability at ϕ_P for different coarse-graining lengths. (b) The percolation probability of defect clusters P^∞ as a function of ϕ for different coarse-graining lengths. The horizontal dashed line is the percolation threshold for critical percolation in the 2D square lattice with PBC, and it is shown as a reference.

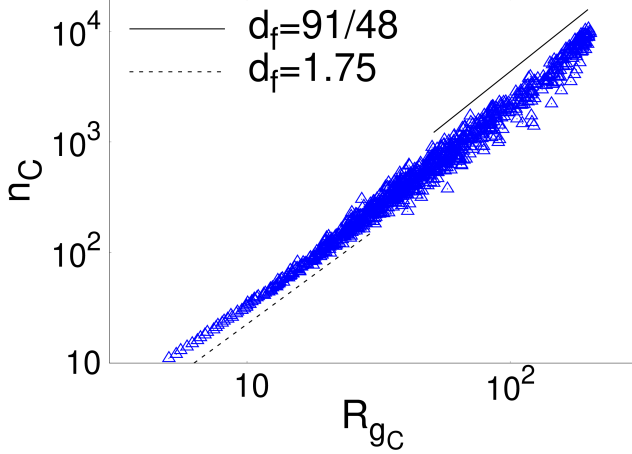


FIG. 35. Scatter plot n_C against the radius of gyration R_{gC} of the defect clusters for $Pe = 50$ and $\phi = \phi_P = 0.815$. The continuous and dashed lines are fits of large ($n_C > 100$) and small ($n_C < 100$) respectively, and the extracted fractal dimensions are reported in the key.

Appendix G: Percolating defect clusters at $Pe = 50$

As illustrated in Sec. VI, we observe percolation of defects at $Pe = 50$ in the dense liquid, close to the high-density branch of MIPS. MIPS inhibits the full statistical development of percolating clusters, and also allows the existence of defect clusters of mixed nature. In this Appendix we provide further details on the morphology of the defect clusters at $Pe = 50$.

The scatter plot in Fig. 35 shows the dependence of the cluster size n_C on the radius of gyration R_{gC} at $\phi = \phi_P$, away from MIPS. We clearly observe that two different kinds of clusters coexist, characterized by a different fractal dimension. On the one hand, large clusters of size $n_C \gtrsim 100$ have fractal dimension $d_f \simeq 91/48$, related to the critical decay exponent of the cluster size distribution shown in Fig. 22, as expected in the context of the percolation transition. On the other hand, grain-boundary structures of fractal dimension $d_f \simeq 1.75$ prevail at smaller scales, capturing the presence of particle aggregation in the dense liquid (see Table III). This behavior shows how MIPS is partially preempting percolation at this Pe , providing a clear picture of the complete disappearance of percolation at larger Pe numbers.

-
- [1] N. D. Mermin and H. Wagner, Phys. Rev. Lett. **17**, 1133 (1966).
 - [2] N. D. Mermin, Phys. Rev. **176**, 250 (1968).
 - [3] V. Berezinskii, Sov. Phys. JETP **32**, 493 (1971).
 - [4] J. M. Kosterlitz and D. J. Thouless, J. Phys. C: Solid State Physics **6**, 1181 (1973).
 - [5] K. J. Strandburg, Rev. Mod. Phys. **60**, 161 (1988).
 - [6] M. A. Glaser and N. A. Clark, Adv. Chem. Phys. **83**, 543 (1992).
 - [7] H. H. von Grünberg, P. Keim, and G. Maret, in *Soft Matter vol. 3*, edited by G. Gompper and M. Schick (John Wiley & Sons, 2007).
 - [8] U. Gasser, J. Phys. Condens. Matter **21**, 203101 (2009).
 - [9] U. Gasser, C. Eisenmann, G. Maret, and P. Keim, ChemPhysChem **11**, 963 (2010).
 - [10] F. Wang, D. Zhou, and Y. Han, Adv. Funct. Mater. **26**, 8903 (2016).
 - [11] B. I. Halperin and D. R. Nelson, Phys. Rev. Lett. **41**, 121 (1978).
 - [12] D. R. Nelson and B. I. Halperin, Phys. Rev. B **19**, 2457 (1979).
 - [13] A. P. Young, Phys. Rev. B **19**, 1855 (1979).
 - [14] K. Zahn, R. Lenke, and G. Maret, Phys. Rev. Lett. **82**, 2721 (1999).
 - [15] K. Chen, T. Kaplan, and M. Mostoller, Phys. Rev. Lett. **74**, 4019 (1995).
 - [16] S. Prestipino, F. Saija, and P. V. Giaquinta, Phys. Rev. E **71**, 050102 (2005).
 - [17] W.-K. Qi, Z. Wang, Y. Han, and Y. Chen, J. Chem. Phys. **133**, 234508 (2010).
 - [18] K. Wierschem and E. Manousakis, Phys. Rev. B **83**, 214108 (2011).
 - [19] S. Chui, Phys. Rev. Lett. **48**, 933 (1982).
 - [20] S. Chui, Phys. Rev. B **28**, 178 (1983).
 - [21] H. Kleinert, Phys. Lett. A **95**, 381 (1983).
 - [22] E. P. Bernard and W. Krauth, Phys. Rev. Lett. **107**, 155704 (2011).
 - [23] S. C. Kapfer and W. Krauth, Phys. Rev. Lett. **114**, 035702 (2015).
 - [24] P. Digregorio, D. Levis, A. Suma, L. F. Cugliandolo, G. Gonnella, and I. Pagonabarraga, Phys. Rev. Lett. **121**, 098003 (2018).
 - [25] W. Qi, A. P. Gantapara, and M. Dijkstra, Soft Matter **10**, 5449 (2014).
 - [26] Y.-W. Li and M. P. Ciamarra, Phys. Rev. E **102**, 062101 (2020).
 - [27] S. S. Khali, D. Chakraborty, and D. Chaudhuri, Soft Matter **17**, 3473 (2021).
 - [28] J. Delhommelle, Phys. Rev. B **69**, 144117 (2004).
 - [29] A. L. Thorneywork, J. L. Abbott, D. G. A. L. Aarts, and R. P. A. Dullens, Phys. Rev. Lett. **118**, 158001 (2017).
 - [30] A. M. Alsayed, M. F. Islam, J. Zhang, P. J. Collings, and A. G. Yodh, Science **309**, 1207 (2005).
 - [31] M. Mazars, EPL **110**, 26003 (2015).
 - [32] M. Mazars and R. Salazar, EPL **126**, 56002 (2019).
 - [33] D. A. Fletcher and P. L. Geissler, Ann. Rev. Phys. Chem. **60**, 469 (2009).
 - [34] G. I. Menon, in *Rheology of Complex Fluids*, edited by A. P. Deshpande, J. M. Krishnan, and P. B. S. Kumar (Madras, India, 2010) p. 193.
 - [35] T. Vicsek and A. Zafeiris, Phys. Rep. **517**, 71 (2012).
 - [36] P. Romanczuk, M. Bär, W. Ebeling, B. Lindner, and L. Schimansky-Geier, Eur. Phys. J. Spec. Topics **202**, 1

- (2012).
- [37] M. E. Cates, Rep. Prog. Phys. **75**, 042601 (2012).
- [38] S. Ramaswamy, Ann. Rev. Cond. Matter Phys. **1**, 323 (2010).
- [39] M. C. Marchetti, J.-F. Joanny, S. Ramaswamy, T. B. Liverpool, J. Prost, M. Rao, and R. A. Simha, Rev. Mod. Phys. **85**, 1143 (2013).
- [40] G. de Magistris and D. Marenduzzo, Physica A **418**, 65 (2015).
- [41] M. E. Cates and J. Tailleur, Annu. Rev. Cond. Matt. Phys. **6**, 219 (2015).
- [42] C. Bechinger, R. D. Leonardo, H. Löwen, C. Reichhardt, G. Volpe, and G. Volpe, Rev. Mod. Phys. **88**, 045006 (2016).
- [43] A. Bernheim-Groswasser, N. S. Gov, S. A. Safran, and S. Tzliil, Advanced Materials **30**, 1707028 (2018).
- [44] L. F. Cugliandolo and G. Gonnella, “Phases of active matter in two dimensions,” (2018), arXiv:1810.11833, to appear in Active Matter and Non-Equilibrium Statistical Physics, J. Tailleur et al. eds. (Oxford Univ. Press).
- [45] L. Berthier, E. Flenner, and G. Szamel, J. Chem. Phys. **150**, 200901 (2019).
- [46] R. J. Allen and B. Waclaw, Rep. Prog. Phys. **82**, 016601 (2019).
- [47] M. Bär, R. Grossmann, S. Heidenreich, and F. Peruani, Ann. Rev. Cond. Matt. **11**, 441 (2020).
- [48] M. R. Shaebani, A. Wysocki, R. G. Winkler, G. Gompper, and H. Rieger, Nature Rev. Phys. **2**, 181 (2020).
- [49] S. Shankar, A. Souslov, M. J. Bowick, M. C. Marchetti, and V. Vitelli, arXiv preprint arXiv:2010.00364 (2020).
- [50] D. Martin, J. O’Byrne, M. E. Cates, E. Fodor, C. Nardini, J. Tailleur, and F. van Wijland, Phys. Rev. E **103**, 032607 (2021).
- [51] J. Tailleur and M. E. Cates, Phys. Rev. Lett. **100**, 218103 (2008).
- [52] Y. Fily and M. C. Marchetti, Phys. Rev. Lett. **108**, 235702 (2012).
- [53] G. S. Redner, M. F. Hagan, and A. Baskaran, Phys. Rev. Lett. **110**, 055701 (2013).
- [54] J. Bialké, H. Löwen, and T. Speck, EPL **103**, 30008 (2013).
- [55] J. Stenhammar, D. Marenduzzo, R. J. Allen, and M. E. Cates, Soft Matter **10**, 1489 (2014).
- [56] A. Wysocki, R. G. Winkler, and G. Gompper, EPL **105**, 48004 (2014).
- [57] J. U. Klamser, S. C. Kapfer, and W. Krauth, Nat. Commun. **9**, 5045 (2018).
- [58] C. A. Weber, C. Bock, and E. Frey, Phys. Rev. Lett. **112**, 168301 (2014).
- [59] S. Paliwal and M. Dijkstra, Phys. Rev. Research **2**, 012013 (2020).
- [60] E. S. Bililign, F. B. Usabiaga, Y. A. Ganan, V. Soni, S. Magkiriadou, M. J. Shelley, D. Bartolo, and W. Irvine, arXiv preprint arXiv:2102.03263 (2021).
- [61] Y. Rouzairé and D. Levis, arXiv preprint arXiv:2103.12578 (2021).
- [62] S. P. Thampi, R. Golestanian, and J. M. Yeomans, EPL **105**, 18001 (2014).
- [63] S. P. Thampi, R. Golestanian, and J. M. Yeomans, Phil. Trans. R. Soc. A **372**, 20130366 (2014).
- [64] L. M. Pismen, Phys. Rev. E **88**, 050502(R) (2013).
- [65] L. Giomi, M. J. Bowick, X. Ma, and M. C. Marchetti, Phys. Rev. Lett. **110**, 228101 (2013).
- [66] L. Giomi, M. J. Bowick, X. Ma, and M. C. Marchetti, Phys. Rev. Lett. **111**, 209901(E) (2013).
- [67] L. Giomi, Phil. Trans. R. Soc. A **372**, 20130365 (2014).
- [68] S. Shankar, S. Ramaswamy, M. C. Marchetti, and M. J. Bowick, Phys. Rev. Lett. **121**, 108002 (2018).
- [69] S. Shankar and M. C. Marchetti, Phys. Rev. X **9**, 041047 (2019).
- [70] B. ten Hagen, S. van Teeffelen, and H. Löwen, J. Phys. Condens. Matter **23**, 194119 (2011).
- [71] P. Romanczuk, M. Bär, W. Ebeling, B. Lindner, and L. Schimansky-Geier, Eur. Phys. J. Spec. Top. **202**, 1 (2012).
- [72] A. Pertsinidis and X. Ling, Phys. Rev. Lett. **87**, 098303 (2001).
- [73] A. Coniglio, L. De Arcangelis, E. Del Gado, A. Fierro, and N. Sator, J. Phys.: Cond. Matt. **16**, S4831 (2004).
- [74] L. Bai and D. Breen, J. Graphics Tools **13**, 53 (2008).
- [75] J. Machta, Y. S. Choi, A. Lucke, T. Schweizer, and L. M. Chayes, Phys. Rev. E **54**, 1332 (1996).
- [76] M. E. J. Newman and R. M. Ziff, Phys. Rev. E **64**, 016706 (2001).
- [77] D. Stauffer and A. Aharony, *Introduction to percolation theory* (Taylor & Francis, 2018).
- [78] D. M. Heyes and J. R. Melrose, Mol. Phys. **66**, 1057 (1989).
- [79] D. M. Heyes and J. R. Melrose, Mol. Phys. **68**, 359 (1989).
- [80] J. Škvor and I. Nezbeda, Phys. Rev. E **79**, 041141 (2009).
- [81] J. M. Kosterlitz, J. Phys. C **7**, 1046 (1974).
- [82] Y. Tang, A. J. Armstrong, R. C. Mockler, and W. J. O’Sullivan, Phys. Rev. Lett. **62**, 2401 (1989).
- [83] Y. Tang, A. J. Armstrong, R. C. Mockler, and W. J. O’Sullivan, Phase Transitions **21**, 75 (1990).
- [84] R. Gupta, J. Delapp, G. G. Batrouni, G. C. Fox, C. F. Baillie, and J. Apostolakis, Phys. Rev. Lett. **61**, 1996 (1998).
- [85] Y. Han, N. Y. Ha, A. M. Alsayed, and A. G. Yodh, Phys. Rev. E **77**, 041406 (2008).
- [86] J. A. Anderson, J. Antonaglia, J. A. Millan, M. Engel, and S. C. Glotzer, Phys. Rev. X **7**, 021001 (2017).
- [87] C. J. Foster, P. B. Blakie, and M. J. Davis, Phys. Rev. A **81**, 023623 (2010).
- [88] J. Jeggle, J. Stenhammar, and R. Wittkowski, J. Chem. Phys. **152**, 194903 (2020).
- [89] A. Poncet, O. Bénichou, V. Démery, and D. Nishiguchi, Phys. Rev. E **103**, 012605 (2021).
- [90] L. Caprini, U. M. B. Marconi, and A. Puglisi, Phys. Rev. Lett. **124**, 078001 (2020).
- [91] S. Hermann, D. de las Heras, and M. Schmidt, Mol. Phys. , e1902585 (2021).
- [92] J. Martín-Roca, R. Martínez, L. C. Alexander, A. L. Diez, D. G. A. L. Aarts, F. Alarcón, J. Ramírez, and C. Valeriani, J. Chem. Phys. **154**, 164901 (2021).
- [93] F. Dittrich, T. Speck, and P. Virnau, Eur. Phys. J. E **44**, 53 (2021).
- [94] C. Maggi, M. Paoluzzi, A. Crisanti, E. Zaccarelli, and N. Gnan, Soft Matter **17**, 3807 (2021).
- [95] C. B. Caporusso, L. Digregorio, D. Levis, L. F. Cugliandolo, and G. Gonnella, Phys. Rev. Lett. **125**, 178004 (2020).
- [96] D. Levis, J. Codina, and I. Pagonabarraga, Soft Matter **13**, 8113 (2017).
- [97] X. Shi, G. Fausti, H. Chaté, C. Nardini, and A. Solon, Phys. Rev. Lett. **125**, 168001 (2020).

- [98] C. B. Caporusso, (2021), private communication.
- [99] H. T. Pinson, *J. Stat. Phys.* **75**, 1167 (1994).
- [100] B. Partridge and C. F. Lee, *Phys. Rev. Lett.* **123**, 068002 (2019).
- [101] C. M. Fortuin and P. W. Kasteleyn, *Physica* **57**, 536 (1972).
- [102] M. Picco, (2019), private communication.
- [103] C. A. Murray and D. H. van Winkle, *Phys. Rev. Lett.* **58**, 1200 (1987).
- [104] R. E. Kusner, J. A. Mann, J. Kerins, and A. J. Dahm, *Phys. Rev. Lett.* **73**, 3113 (1994).
- [105] I. Guillamón, H. Suderow, A. Fernández-Pacheco, J. Sesé, R. Córdoba, J. M. D. Teresa, M. R. Ibarra, and S. Vieira, *Nature Phys.* **5**, 651 (2009).
- [106] J. M. Kosterlitz and D. J. Thouless, *J. Phys. C: Solid State Physics* **6**, 1181 (1973).
- [107] Y. W. Li and M. P. Ciamarra, *Phys. Rev. Lett.* **124**, 218002 (2020).
- [108] Y. W. Li and M. P. Ciamarra, *Phys. Rev. E* **102**, 062101 (2020).
- [109] L. A. Padilla and A. Ramírez-Hernández, *J. Phys.: Cond. Matt.* **32**, 275103 (2020).
- [110] G. Dagvadorj, M. Kulczykowski, M. H. Szymanska, and M. Matuszewski, “First-order dissipative phase transition in an exciton-polariton condensate,” (2021), arXiv:2104.07385.
- [111] P. Bladon and D. Frenkel, *Phys. Rev. Lett.* **74**, 2519 (1995).
- [112] W. Qi, A. P. Gantapara, and M. Dijkstra, *Soft Matter* **10**, 5449 (2014).
- [113] C. Reichhardt and C. J. Olson Reichhardt, *Phys. Rev. Lett.* **90**, 095504 (2003).
- [114] A. Zippelius, B. I. Halperin, and D. R. Nelson, *Phys. Rev. B* **22**, 2514 (1980).
- [115] C. M. Fortuin, *Physica* **58**, 393 (1972).
- [116] C. M. Fortuin, *Physica* **59**, 545 (1972).
- [117] N. Sator, *Phys. Rep.* **376**, 1 (2003).
- [118] M. Ester, H.-P. Kriegel, J. Sander, and X. Xu, in *Proceedings of the Second International Conference on Knowledge Discovery and Data Mining (AAAI, 1996)*.
- [119] A. Jelić and L. F. Cugliandolo, *J. Stat. Mech.* **2011**, P02032 (2011).